ADVANCED FUNCTIONAL MATERIALS
www.afm-journal.de

# The Influence of Annealing on the Sb Layer in the Synthesis of [001]-Oriented $Sb_2Se_3$ Film for Photoelectrochemical Hydrogen Gas Generation

*Magno B. Costa, Moisés A. de Araújo, Joaquim Puigdollers, Pablo Ortega, Teresa Andreu, Cristobal Voz, Edgardo Saucedo,* and Lucia H. Mascaro**

**This work reports a new thermal treatment approach to obtain [001]-oriented $Sb_2Se_3$ film, which consists of preliminary annealing of the Sb layer before its selenization. Among the different Sb annealing temperatures assessed, the one at 200 °C followed by selenization ($Sb_2Se_3$(Sb-A200)) results in a considerably high texture coefficient at the [001] direction, whereas the $Sb_2Se_3$ film obtained only by selenization of the non-annealed Sb film ($Sb_2Se_3$(Sb-NA)) features preferential orientation at the [*hk*0] direction. In terms of photoelectrochemical (PEC) performance for $H_2$ generation, the $Sb_2Se_3$(Sb-A200)/CdS/$TiO_2$/Pt film delivers a substantial photocurrent density of −5.65 mA $cm^{-2}$ at 0 $V_{RHE}$, which is 10 times higher compared to the $Sb_2Se_3$(Sb-NA)/CdS/$TiO_2$/Pt film. Additionally, the employment of the Sb annealing step results in stable PEC performance of the $Sb_2Se_3$ film over 7000 s, meaning that the photocorrosion is minimized. The improved PEC performance of the $Sb_2Se_3$ film is attributed to better crystallinity and composition closer to the stoichiometric condition, as well as the preferential orientation at the [001] direction that favors charger carriers' transportation. At last, the findings of this work feature an innovative thermal treatment approach to obtain [001]-oriented $Sb_2Se_3$ film to further improve $H_2$ generation from PEC water splitting.**

## 1. Introduction

The concern of depletion of energy resources based on fossil fuels has led lately to a considerable increase in the search for renewable energy sources that can potentially replace them. More worrying is that fossil fuel resources contribute about 90% of global energy consumption, which impacts the increase in the emission of carbon dioxide ($CO_2$) into the atmosphere.[1] Although $CO_2$ is an essential gas for the maintenance of life, the ever-growing release of this gas into the atmosphere, from fossil fuel combustion, can considerably contribute to the intensification of the greenhouse effect and climate changes, and these can cause an increase in the average temperature of the planet and affect the entire existing ecosystem.[2] To circumvent these problems, sunlight has become one of the most promising alternative energy resources due to being abundant and environmentally friendly, ease of usage/harvest, less overall cost, and versatile.[3,4] Additionally, solar energy can be converted to thermal energy via solar water heaters, or electrical and chemical energy via photovoltaic and PEC devices, respectively.[5] The conversion of solar energy into chemical energy consists of storing energy in the bonds of hydrogen gas ($H_2$) molecules, and this molecule is known as a dense energy carrier. $H_2$ has heat capacity and energy density much higher than batteries,[6,7] and the energy yield

M. B. Costa, L. H. Mascaro
Departamento de Química
Universidade Federal de São Carlos (UFSCar)
Rodovia Washington Luiz, km 235, São Carlos, São Paulo 3565-905, Brazil
E-mail: lmascaro@ufscar.br
M. A. de Araújo
Instituto de Química de São Carlos
Universidade de São Paulo (USP)
Avenida Trabalhador Sancarlense, 400, São Carlos, São Paulo 13566-590, Brazil
The ORCID identification number(s) for the author(s) of this article can be found under https://doi.org/10.1002/adfm.202506401



**DOI: 10.1002/adfm.202506401**

J. Puigdollers, P. Ortega, C. Voz, E. Saucedo
Electronic Engineering Department
Universitat Politècnica de Catalunya (UPC)
Micro and Nano Technologies Group (MNT)
Jordi Girona 31, Barcelona 08034, Spain
E-mail: edgardo.saucedo@upc.edu
M. B. Costa, J. Puigdollers, E. Saucedo
Barcelona Center for Multiscale Science & Engineering
Universitat Politècnica de Catalunya (UPC)
Av Eduard Maristany 10-14, Barcelona 08019, Spain
T. Andreu
Departament de Ciència dels Materials i Química Física
Universitat de Barcelona (UB)
Martí i Franquès, 1, Barcelona 08028, Spain

of $H_2$ is 2.75 times higher compared to that of hydrocarbon fuels.[8] One way to obtain $H_2$ is via solar water splitting, which can be carried out in PEC cells or photovoltaic panels coupled to electrolyzers.[7]

To drive solar water splitting into PEC cells, a variety of semiconductor materials have been under investigation, and among those antimony(III) selenide ($Sb_2Se_3$) thin film has stood out as a promising photocathode owing to its adequate intrinsic optoelectronic properties, earth-abundant elements, and low toxicity.[9,10] To exemplify the optoelectronic properties of $Sb_2Se_3$, this material has a high absorption coefficient, $a$, in the ultraviolet and the visible region of the solar spectrum ($a > 10^5\ cm^{-1}$),[11] suitable optical bandgap energy, $E_g$, of 1.1–1.3 eV,[12–14] high mobility (≈10 $cm^2\ V^{-1}\ s^{-1}$ for minority carriers),[15] long carrier lifetime (≈60 ns),[15] and appropriate energy band position to drive hydrogen evolution reaction (HER) under illumination.[14,16,17] In addition, $Sb_2Se_3$ has a single orthorhombic crystalline phase composed of quasi-1D (Q1D) parallel ribbons of $(Sb_4Se_6)_n$ in one spatial direction.[18,19] These Q1D $(Sb_4Se_6)_n$ ribbons present covalent Sb−Se bonds along the [001] direction, and the ribbons are stacked along the [100] and [010] directions, which are held together by van der Waals forces.[20] The different orientation growth of the $(Sb_4Se_6)_n$ ribbons enables the existence of anisotropic crystallographic behavior, meaning that any preferred orientation in the [001] direction (ribbons vertically oriented to the substrate) favors the charge transport, as the charge carriers travel more easily along the ribbon-like structure. On the other hand, the $(Sb_4Se_6)_n$ ribbons featuring [100] and [010] directions (ribbons horizontally oriented to the substrate) result in difficulty for charge carriers transport due to the hopping mechanism, that is, charge carriers must hop from one $(Sb_4Se_6)_n$ ribbon to another.[20] Such an anisotropic charge carriers' transportation suggests that a properly textured $Sb_2Se_3$ film (i.e., featuring [$hk$1] direction) is the ideal condition for solar energy conversion applications.[20–22] Additionally, the combination of all these properties makes $Sb_2Se_3$ a very promising semiconductor material to be used as a photocathode for PEC cells when compared to other semiconductors.[23–25]

Although $Sb_2Se_3$ has been extensively demonstrated to be an excellent alternative as a photocathode for solar-driven water splitting,[26,27] the electron-hole recombination process in bulk, and the presence of interfacial defects are recurrent issues[18] that limit to reach satisfactory PEC performance of this material for commercial application.[28] To overcome these issues, the improvement of crystallinity and the control of elemental composition of $Sb_2Se_3$ have been attributed as the main factors to enhance the PEC performance of $Sb_2Se_3$ photocathode.[29,30] Regarding, particularly the elemental composition effect, Caño et al.[31] have recently shown that nonstoichiometric Mo/$Sb_2Se_3$ film gives rise to secondary phases, that is, Se-rich Mo/$Sb_2Se_3$ film leads to the formation of $MoSe_2$ and Se phases, whereas the Sb-rich condition favors the occurrence of $Sb_2O_3$ and m-Sb phases. In another recent study, Lian et al.[32] identified the presence of deep-level defects in Sb-rich $Sb_2Se_3$ film, which, based on experimental results, were characterized as amphoteric $Sb_{Se}$ defects. Moreover, according to the authors, the amphoteric defects in this material can trap both electrons and holes, resulting eventually in a recombination process. It was also shown that Se-rich $Sb_2Se_3$ films have relatively less defect concentration as well as a reduced number of shallow energy levels. Besides the elemental composition effect, another limiting factor is that the [$hk$1]-oriented $Sb_2Se_3$, which is the ideal condition for PEC and photovoltaic cells, is not thermodynamically favorable compared to that of [$hk$0] orientation, as the [$hk$0] leads to the formation of $Sb_2Se_3$ crystal facets with a lower formation energy.[33]

To tackle this issue, studies have recently shown that [$hk$1]-oriented $Sb_2Se_3$ film can be obtained by optimizing the selenization temperature of either the Sb or $Sb_2Se_3$ film.[34,35] It is often reported that the employment of molybdenum (Mo) as the back-contact to grow [$hk$1]-oriented $Sb_2Se_3$ film during the selenization step, however, Liang et al.[36] demonstrated that the in situ surface selenization of tungsten (W) can be used as a back-contact to enable the obtainment of $Sb_2Se_3$ film featuring [$hk$1] preferred orientation. Furthermore, the authors reported that the thin layer of $WSe_2$ behaves as a hole transport layer, which means that this material can collect the photogenerated holes and block the photogenerated electrons from transferring to the back-contact, hindering the electron-hole recombination process.

Herein, it is considered an alternative thermal treatment approach to obtain [001]-oriented $Sb_2Se_3$ film. For this study, a new methodology was developed consisting of preliminary annealing of the Sb layer before the selenization step. Particularly, it was aimed to investigate the influence of the different annealing temperatures of the Sb layer and the different selenization conditions (i.e., temperature and dwelling time) of the annealed Sb layer to produce [001]-oriented $Sb_2Se_3$ film. It was also targeted to assess how the crystallinity and elemental composition of the [001]-oriented $Sb_2Se_3$ film directly affect the PEC performance for $H_2$ production via solar-driven water splitting. As will be shown in the Results and Discussion section, compared to the $Sb_2Se_3$ film obtained only via selenization, the annealing of the Sb layer before selenization led to the formation of $Sb_2Se_3$ film with preferential crystallographic orientation to the [001] direction, better crystallinity, and suitable elemental composition. It will also be demonstrated that the $Sb_2Se_3$ film obtained via annealing of Sb before selenization delivers a substantial improvement of PEC activity and stability for $H_2$ generation from the water splitting reaction. All in all, the annealing step developed in this work provides an alternative approach to considerably enhance PEC activity and stability of [001]-oriented $Sb_2Se_3$ film for $H_2$ production.

## 2. Results and Discussion

### 2.1. Characterization of Single-Layered Films

#### *2.1.1. Selenization of Non-Annealed Sb*

In this regard, the elemental composition of the $Sb_2Se_3$(Sb-NA) film submitted to selenization at 320 °C for 30 min was analyzed by XRF. According to Figure S3a, Supporting Information, the elemental composition of the film was Se-rich, presenting a maximum atomic percentage ratio of 3[Sb%]/2[Se%] ≈ 0.67, which is far from the stoichiometric value (3[Sb%]/2[Se%] = 1, corresponding to 60 at.% Se and 40 at.% Sb). A brief investigation was performed over the range of selenization temperatures of 320 ± 20 °C (i.e., 300 and 340 °C for 30 min), however, the films continued to present a Se-rich composition. Se-rich $Sb_2Se_3$ films have also been reported as an effective stoichiometric condition

for photovoltaic cell application due to the presence of benign defects, that is, $Se_{Sb}$ antisites (shallow acceptors) and the difficulty of detrimental defects formation, such as selenium vacancies and $Sb_{Se}$ antisites (deep donors).[37–39]

### 2.1.2. Annealing Temperature Effect of Sb

In the attempt to find out the reason for obtaining Se-rich $Sb_2Se_3$(Sb-NA) films, XRD measurements were performed for the as-deposited Sb film not subjected to annealing step (labeled as Sb-NA), as well as for those annealed at 150, 200, and 250 °C for 30 min (labeled as Sb-A150, Sb-A200, and Sb-A250, respectively). As shown in Figure S3b, Supporting Information, it was identified weak reflections for the (003), (006), and (202) planes of the Sb-NA film, which were assigned to the rhombohedral Sb phase (Powder Diffraction File (PDF) no. 35–732). These peaks featured low intensity, suggesting poor crystallinity of the Sb-NA film. That may have prevented the formation of a more stoichiometric $Sb_2Se_3$ film and affected its composition during the selenization process. However, the results for the as-deposited Sb films annealed at the highest temperatures, namely, Sb-A200 and Sb-A250 films, showed strong reflections and therefore more crystalline films compared to those of the Sb-NA and Sb-A150 films, which have weak reflections.

As additional evidence of the annealing effect, it can be observed that a decrease of up to 21.5% of the full width at half maximum (FWHM) values for the (006) plane (Figure S3c, Supporting Information), indicating an increase in the size of the Sb crystallite as the annealing temperature increases. Interestingly, the Sb-A200 and Sb-A250 films featured a secondary phase of $Sb_2O_3$ (PDF no. 75–1565) as noted by the peaks indexed to the (111), (222), and (444) planes, which are indicated by circled regions in the XRD patterns (cf. Figure S3b, Supporting Information). Although the annealing was performed under Ar atmosphere, this result indicates that the Sb films underwent thermal oxidation at annealing temperatures higher than 200 °C. Despite the presence of the $Sb_2O_3$ secondary phase, the selenization process (performed at 320 °C) can convert all oxidized phases into $Sb_2Se_3$. According to Equations (1) and (2), which consider the reaction between $Sb_{(s)}$ and $Se_{(g)}$, and the reaction of $Sb_{(s)}$ and $O_{2(g)}$ both at 320 °C (corresponds to 593 K),[40,41] the formation of $Sb_2Se_3$ is thermodynamically more favorable than $Sb_2O_3$ and the selenization also allows any oxide residues to be converted into the $Sb_2Se_3$. Furthermore, elementary Se has a melting point of 221 °C,[42] and high vapor pressure,[43] which contributes to the chalconization in the absence of oxygen gas. The reader is referred to the Supporting Information (SI) for details about the calculation of the values of the molar Gibbs energy of reaction at 593 K ($\Delta_r G$(593 K)) for the reactions in Equations (1) and (2).

$$2Sb_{(s)} + 3Se_{(g)} \rightarrow Sb_2Se_{3(s)} \quad \Delta_r G\ (593\ K) = -670.9\ kJ\ mol^{-1} \quad (1)$$

$$2Sb_{(s)} + \frac{3}{2}O_{2(g)} \rightarrow Sb_2O_{3(s)} \quad \Delta_r G\ (593\ K) = -546.8\ kJ\ mol^{-1} \quad (2)$$

### 2.1.3. Selenization of Sb Annealed at Different Temperatures

The as-deposited Sb films annealed at different temperatures were subsequently submitted to selenization and assessed their elemental composition by the XRF analysis (**Figure 1a**). It is possible to observe that the annealing of the Sb improved the stoichiometry of the $Sb_2Se_3$ films, allowing the 3[Sb%]/2[Se%] atomic ratio of these films to increase compared to those of the $Sb_2Se_3$ films obtained without annealing the Sb. This is indicative that more crystalline Sb films may lead to better formation of $Sb_2Se_3$ phase in the selenization process. The best annealing condition before selenization was at 200 °C, as favored a maximum 3[Sb%]/2[Se%] atomic ratio of ≈0.8. The improvement of adjusted chemical composition might be attributed to a lesser extent elemental Se condensation over the surface of the $Sb_2Se_3$(Sb-A) films compared to those of $Sb_2Se_3$(Sb-NA) films. The elemental Se condensation may have occurred during the selenization process of the Sb-A and Sb-NA films.[44] The presence of elemental Se on the $Sb_2Se_3$(Sb-A) films' surface was verified by XPS analysis (see discussion further). The minimized condensation of elemental Se for the $Sb_2Se_3$(Sb-A) films might be associated with the crystal structure of the [001]-oriented Sb-A films (see discussion of Figure 1b,c) that possibly favors diffusion of sublimated Se atoms into the [001]-oriented crystal lattice of the Sb-A film that can subsequently react to form [001]-oriented $Sb_2Se_3$.[45]

The $Sb_2Se_3$ films obtained via selenization of annealed Sb, as well as the $Sb_2Se_3$(Sb-NA) film, were also characterized by XRD measurements (see Figure 1b). All the diffractograms featured diffraction peaks indexed to the (020), (120), (220), (230), (211), (221), (301), (311), (240), (231), (141), (411), (002) and (061) planes, and these peaks were assigned to the orthorhombic $Sb_2Se_3$ phase (PDF no. 89–821). The diffraction peaks labeled with asterisks (*) are attributed to the Mo-coated glass substrates (PDF no. 42–1120). Furthermore, it was not identified the diffraction peaks of the secondary phase of $Sb_2O_3$, proved the efficacy of the method of fully converting the Sb and $Sb_2O_3$ phases into the $Sb_2Se_3$ phase during selenization, as shown in Equations (1) and (2). Another interesting aspect from Figure 1b is that all the $Sb_2Se_3$ films obtained via selenization of the annealed Sb showed strong reflections for the (002) plane compared to those of the $Sb_2Se_3$(Sb-NA) film, indicating better crystallinity and preferential orientation in the [001] direction. To better understand the preferred orientation of the crystallographic planes of the $Sb_2Se_3$ films, the texture coefficient for a given (*hkl*) plane, TC(*hkl*), was calculated using Equation (3),[27] and the results are displayed in Figure 1c.

$$TC\ (hkl) = \frac{I_{(hkl)}}{I_{0(hkl)}} \left\{ \frac{1}{N} \sum_{i=0}^{N} \frac{I_{(hkl)}}{I_{0(hkl)}} \right\}^{-1} \quad (3)$$

where $I_{(hkl)}$ and $I_{0(hkl)}$ are the diffraction peak intensities for a given (*hkl*) plane measured from the XRD and the database of XRD ($Sb_2Se_3$ PDF no. 89–821) patterns, respectively, and $N$ is the number of planes considered for the calculation (10 planes in that diffractogram).

According to Figure 1c, the TC for the (120), (301), (221), and (211) planes featured similar values and were lower than 1, meaning no preferential crystal orientation for these planes. However, TC(230) > 1 was achieved for the $Sb_2Se_3$(Sb-NA) and $Sb_2Se_3$(Sb-A150) films, suggesting that the crystal of $Sb_2Se_3$ has a preferential growth orientation parallel to the substrate ([100] and/or [010] orientation), which is not efficient for photogenerated charge

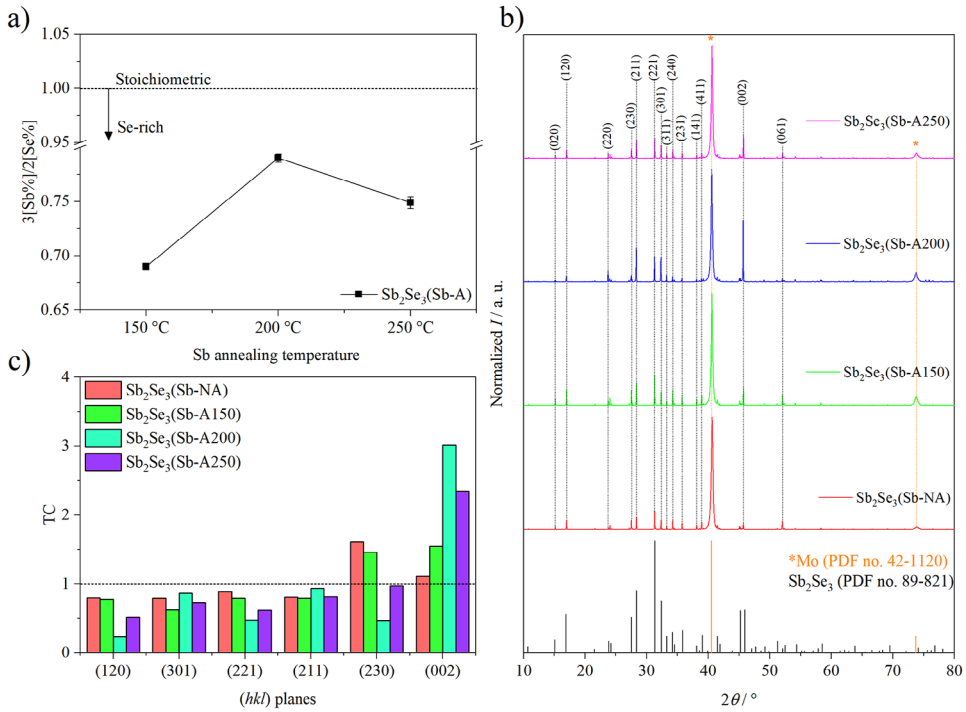


**Figure 1.** a) Atomic percentage ratio obtained from the XRF analysis, b) XRD patterns, and c) TC(*hkl*) values of the $Sb_2Se_3$ (Sb-NA) and the $Sb_2Se_3$ (Sb-A) films. XRD patterns of the PDF database for the orthorhombic $Sb_2Se_3$ (PDF no. 89–821) and the cubic Mo (PDF no. 42–1120) phases are displayed as vertical lines at the bottom of the diffractograms. The diffraction peaks labeled with * were assigned to the Mo back-contact.

carriers transportation due to inter-ribbons hopping mechanism. For the (002) plane, the $Sb_2Se_3$(Sb-A200) film featured the highest TC(002) value (i.e., ≈ 3), indicating the ribbons of the $Sb_2Se_3$ are vertically grown to the substrate ([001] orientation), which favor efficient photogenerated charge carriers transportation owing to the transport of the carriers alongside the ribbons. It was also noted that the $Sb_2Se_3$(Sb-A200) film has the lowest value for the TC(120), indicating low contribution of the parallel orientation to the substrate. This preferential growth of the [001] direction for the $Sb_2Se_3$ has likely occurred due to the influence of the improved intensity of the diffraction peaks for the (003) and (006) planes ([001]-oriented Sb) of the Sb-A200 and Sb-A250 films compared to those of the Sb-A150 and Sb-NA films (cf. Figure S3b, Supporting Information). The (003) and (006) planes enable continuous diffusion of sublimated Se to react with [001]-oriented Sb and form column growth of [001]-oriented $Sb_2Se_3$.[45] To better understand this phenomenon in terms of a possible selenization mechanism, the change in temperature during the annealing process directly influences the vapor pressure of Se atoms and their kinetic energy. At a given selenization temperature, the sublimated Se atoms may adsorb on the [001]-oriented Sb film surface with sufficient energy to react and form a $Sb_2Se_3$ crystal nucleus. The sublimated Se atoms may continue to diffuse to the [001]-Sb/[001]-$Sb_2Se_3$ interface along the van Waals gaps of $Sb_2Se_3$ to extend the length of the [001]-$Sb_2Se_3$ preferential growth.[34,46]

However, despite the Sb-A250 film featuring the highest intensity of the Sb's diffraction peaks for the (003) and (006) planes, the presence of the $Sb_2O_3$ phase may have minimized its preferential orientation in the [001] direction compared to that of the $Sb_2Se_3$(Sb-A200) film. Therefore, the experimental condition for the preparation of $Sb_2Se_3$(Sb-A200) film was chosen as the optimum condition.

Additional characterization of the $Sb_2Se_3$(Sb-NA) and the $Sb_2Se_3$(Sb-A) films was achieved by Raman spectra, as shown in **Figure 2**. The main vibrational modes of $Sb_2Se_3$ are represented by well-defined bands within a range of 50 – 300 $cm^{-1}$.[44] The bands located at 210 and 190 $cm^{-1}$ are related to the $A_g$ mode of the Sb–Se–Sb bending vibrations of the $Sb_2Se_3$, while the small band ≈154 $cm^{-1}$ is assigned to the $A_{2u}$ vibration mode of the Sb–Sb bond. The observed bands at 120 and 80 $cm^{-1}$ are attributed to the Se–Se bending.[44,47] It is important to mention that none of the samples displayed the characteristic bands of the $Sb_2O_3$ secondary phase in the Raman spectra (corresponding to the main bands at 254 and 450 $cm^{-1}$[44]), however, all the samples presented low-intensity bands at 98 and 250 $cm^{-1}$ assigned to the presence of $Se_6$ ring (rhombohedral Se).[44,48] It has also been reported that Se-rich chalcogenide film can provide rhombohedral Se signals in that region, which arise from the excess of Se deposited on the samples' surface.[49,50] The Raman spectra in this work suggest that the selenization process may have contributed to the occurrence of elemental Se on the surface of all the samples, and this agrees with the XRF analysis, which indicates that the $Sb_2Se_3$ are Se-rich (cf. Figure 1a). Nevertheless, it was not identified Se phase in the XRD data (cf. Figure 1b), probably indicating that Se phase may be present in small quantities.

Figure S4a,b, Supporting Information show the Tauc plots as $(\alpha h\nu)^{1/2}$ versus $E_{ph}$ (indirect transition) and $(\alpha h\nu)^2$ versus $E_{ph}$ (direct transition), respectively.[51] For an indirect and a direct transition, the linear extrapolation to the baseline rendered optical $E_g$

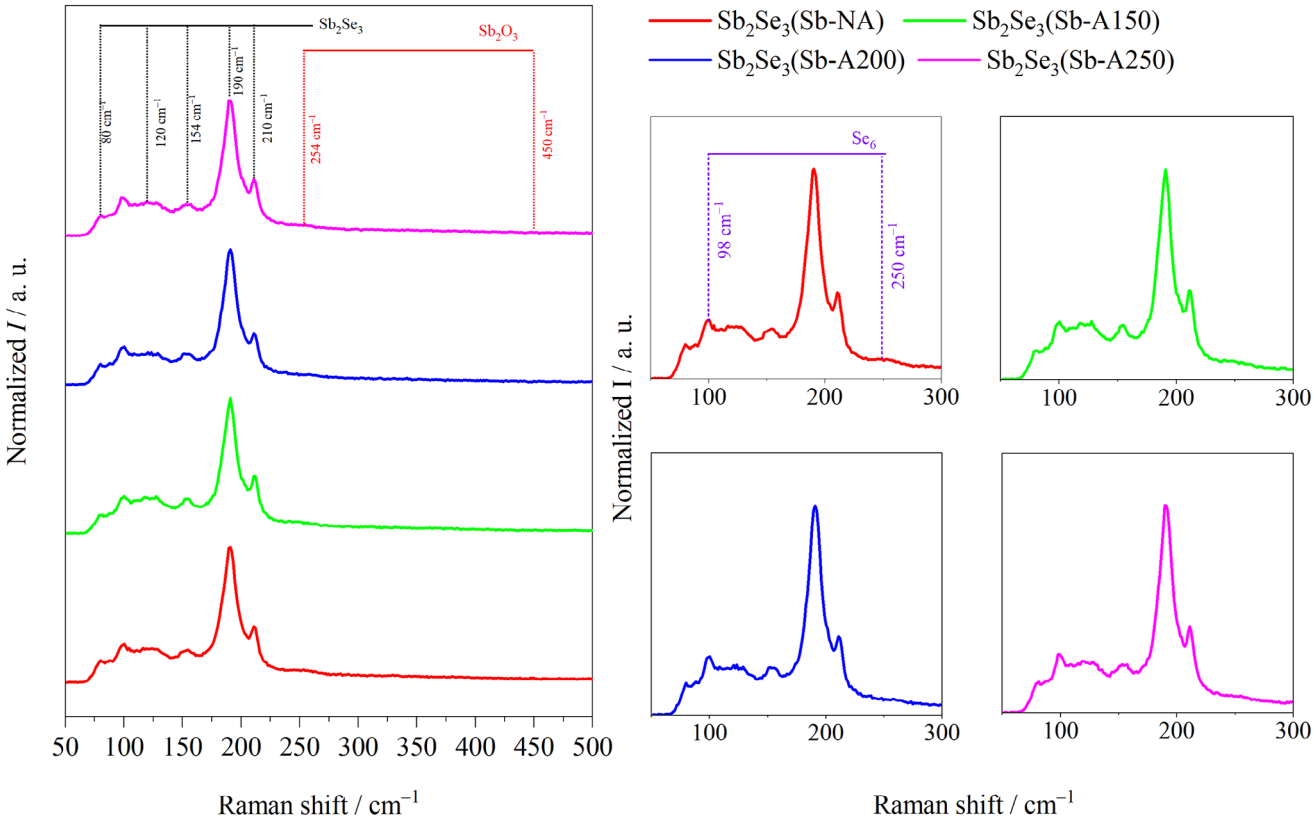


**Figure 2.** (on the left) Raman spectra and their corresponding (on the right) expanded region of the spectra encompassing the main bands of $Sb_2Se_3$ for the $Sb_2Se_3$ (Sb-NA) and the $Sb_2Se_3$ (Sb-A) films.

values of 1.33 and 1.34 eV, respectively, for all the samples. These results are slightly higher than those reported in the literature (i.e., 1.1–1.3 eV[12–14]), however, it is also reported that $Sb_2Se_3$ with higher optical $E_g$ for nanorod[52,53] or nanowires[54] morphologies. In addition, it was also assessed the $E_u$ of the films, which characterizes the structural disorder of the semiconductor.[55] An increase of $E_u$ value represents an enlargement of the width of the bands' edges tail, which means a more pronounced structural disorder in the semiconductor. This parameter can be understood as the width of the tail of the conduction and valence band edges associated with the localized defect states within the $E_g$. Additionally, the presence of the bands' edges tailing corresponds to transitions between extended states of the valence band and localized states of the conduction band.[56] According to Figure S4c, Supporting Information, it can be seen a narrow linear region in the inset of the $E_u$ plot before the $E_g$ values, which the $E_u$ was estimated from the inverse of the slope of the straight lines in the graphs. Unlike the optical $E_g$ value in which there was no difference in comparison with the different samples, the $E_u$ has shown a slight difference in their values. The lowest value of the $E_u$ was 0.21 eV for the $Sb_2Se_3$(Sb-A200) film compared to those of the other films. This indicates that the annealing at 200 °C of the Sb film has contributed to the decrease of the structural disorder and the localized defects in the band edges of the $Sb_2Se_3$(Sb-A200) film. On the other hand, the $Sb_2Se_3$(Sb-A250) film featured the highest value of the $E_u$ (i.e., 0.32 eV), indicating that this film has a higher number of localized defects in its band edges compared to the other films.[57]

The $Sb_2Se_3$(Sb-A200) film, that is, representing the optimum condition, was chemically assessed by the XPS measurements, and the spectra are displayed in **Figure 3**. As shown in Figure 3a, the survey spectrum exhibits the main peaks of Sb, Se, O, and C elements, corresponding to Sb 4p, Sb 3d, Sb 4s, Sb 4d, Se 3s, Se 3p, Se 3d, O 1s, and C 1s core levels, respectively. Regarding the high-resolution XPS spectra (Figure 3b), the spectrum of the Sb 3d core level features two Sb 3d doublets: the first one with peaks at 529 (Sb $3d_{5/2}$) and 538.34 eV (Sb $3d_{3/2}$) are assigned to the Sb–Se bonds in $Sb_2Se_3$, whereas the second one having peaks at 530 (Sb $3d_{5/2}$) and 539.34 eV (Sb $3d_{3/2}$) are attributed to the Sb–O bonds.[58] Since XPS is a highly surface-sensitive technique, the presence of an Sb–O signal is a result of the sample being exposed to air before the XPS analysis,[59] and this has also been reported in the literature.[60–62] The presence of Sb–O signal (possibly $Sb_2O_3$) might be beneficial as it could passivate defects (i.e., Se vacancies) on the surface of $Sb_2Se_3$ films.[62] Moreover, bearing in mind that XPS is surface-sensitive (penetration depth of 10 nm or less[63]), despite the possibility of superficial formation of $Sb_2O_3$, the bulk properties of $Sb_2Se_3$ films remain unaltered, as can be verified from the discussion of XRD (cf. Figure 1) and Raman (cf. Figure 2). Still regarding Figure 3b, The O 1s peak at 531.7 eV is assigned to the adventitious oxygen weakly adsorbed on the surface, which could also be a result of atmospheric $CO_2$ physisorption on the photoelectrode surface.[64] Concerning the

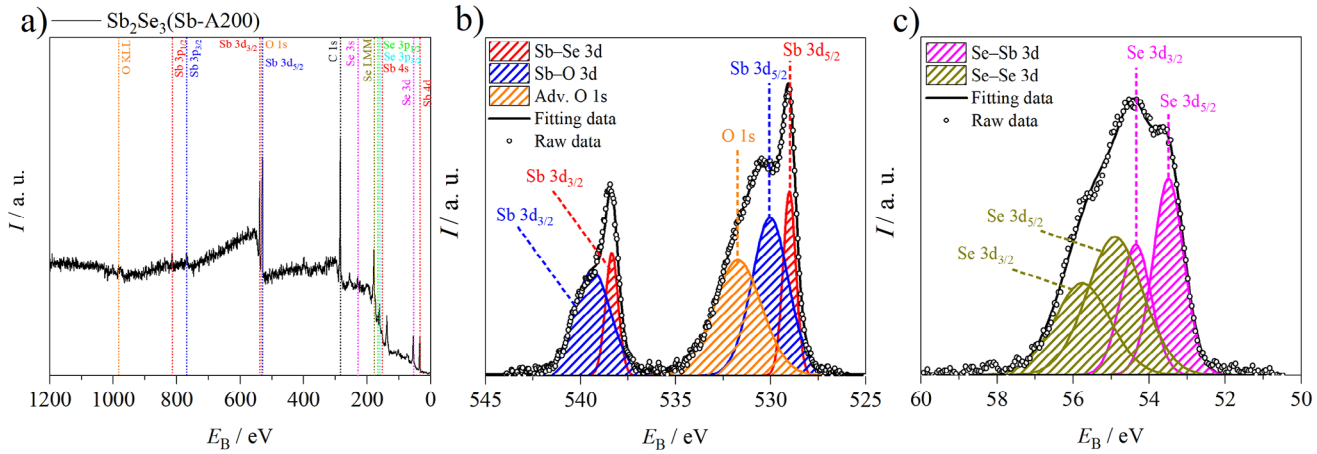


**Figure 3.** a) The survey and high-resolution XPS spectra of b) Sb 3d and c) Se 3d core levels for $Sb_2Se_3$(Sb-A200) film.

high-resolution spectra of the Se 3d core level (Figure 3c), one notices the presence of two Se 3d doublets: the first one containing peaks at 53.5 (Se $3d_{5/2}$) and 54.36 eV (Se $3d_{3/2}$) are assigned to the Se–Sb bonds in $Sb_2Se_3$, and the second one with peaks at 54.9 (Se $3d_{5/2}$) and 55.76 eV (Se $3d_{3/2}$) are attributed to the Se–Se bonds in elemental selenium.[58] As shown in the discussion of the Raman spectra (cf. Figure 2), the presence of elemental selenium arises from the excess of Se in the form of $Se_6$ rings on the samples' surface during the selenization process or even as a side-product of the $Sb_2Se_3$ air oxidation.

Besides the chemical assessment, it has employed SEM analyses (**Figure 4**) to characterize the morphology on the surface and at the cross-section of the $Sb_2Se_3$(Sb-NA) and the $Sb_2Se_3$(Sb-A) films. As indicated in Figure 4a, it is possible to observe the formation of rod-like structures with lengths of more than 1 µm, which are randomly oriented in all directions on the surface of the $Sb_2Se_3$(Sb-NA) film. The presence of these rod-like structures may indicate a preferential orientation of the $Sb_2Se_3$ crystal. Since the $Sb_2Se_3$(Sb-NA) film featured preferential orientation to the (230) plane (cf. Figure 1c), this implies that the rod structures might be associated with the existence of $(Sb_4Se_6)_n$ ribbons oriented at the [*hk*0] direction (i.e., ribbons horizontally oriented to the substrate).[33] For the $Sb_2Se_3$(Sb-A) films (cf. Figure 4a), the $Sb_2Se_3$(Sb-A150) film features a mix of morphologies on its surface, ranging from microrods to round-shaped structures. The morphology of the $Sb_2Se_3$(Sb-A200) film mostly consists of compacted irregular structures, whose contours are well-defined. On the other hand, the morphology of the $Sb_2Se_3$(Sb-A250) film presents a less-defined shape, including elongated and misshapen grains. The cross-section micrographs in Figure 4b showed differences in the films' morphology. The $Sb_2Se_3$(Sb-NA) and $Sb_2Se_3$(Sb-A150) films show less-defined grains, whereas the $Sb_2Se_3$(Sb-A250) film displays voids between the $Sb_2Se_3$ and the tri-layer Mo. For the $Sb_2Se_3$(Sb-A200) film, one notices the presence of homogeneous and well-defined grains vertically grown on the tri-layer Mo with no voids between them. The formation of these vertically oriented structures for the $Sb_2Se_3$(Sb-A200) film suggests formation of [001]-oriented $(Sb_4Se_6)_n$ ribbons,[33] as was also observed by the highest TC(002) value of ≈3 (see Figure 1c). All the morphological features of the $Sb_2Se_3$(Sb-A200) film can be better observed in the micrographs zoomed out of the surface and cross-section (Figure 4c). Regarding the thickness of the films, although it is not possible to accurately measure the thickness due to the non-uniformity, one notices that the thickness of the $Sb_2Se_3$(Sb-A) films is higher compared to that of $Sb_2Se_3$(Sb-NA) film (cf. Figure 4b). This apparent increase in thickness of the $Sb_2Se_3$(Sb-A) films is probably due to enlarged crystallite size of Sb-A films upon the annealing process, which can be observed by the decrease of up to 21.5% of the FWHM values for the (006) plane (Figure S3c, Supporting Information), representing an increase in ≈11 nm (according to the Scherrer equation) of the Sb crystallite size.

### *2.1.4. Optimizing Selenization of Annealed Sb*

According to the results that have been presented so far, the optimum thermal treatment condition corresponded to the sample labeled as $Sb_2Se_3$(Sb-A200). Aiming to further evaluate the thermal treatment approach of the $Sb_2Se_3$ films, it has also been assessed the effect of the selenization on the Sb-A200 films at different temperatures (i.e., 280, 300, 320, and 340 °C) and dwelling times (i.e., 30 and 60 min). The Sb-A200 films selenized at different temperatures and times were characterized in terms of their elemental composition, crystal structure, and photoelectrocatalytic performance toward HER, as presented as follows.

From the XRF analysis (**Figure 5**a), one notices that the Sb-A200 films selenized at the lowest temperature and time (i.e., 280 °C and 30 min, respectively) featured the highest atomic ratio of 0.81, which is reasonably close to the expected stoichiometric value. Additionally, the Se-rich condition became more pronounced for the Sb-A200 films selenized at the highest temperature and time (i.e., 340 °C and 60 min, respectively), leading to a minimum value of atomic ratio of 0.69. Based on these results, one can infer that longer dwelling times and higher temperatures can lead to a sublimated Se-rich atmosphere and significantly affect the composition of the samples. This result means that the employment of the annealing step for the Sb film and the simple

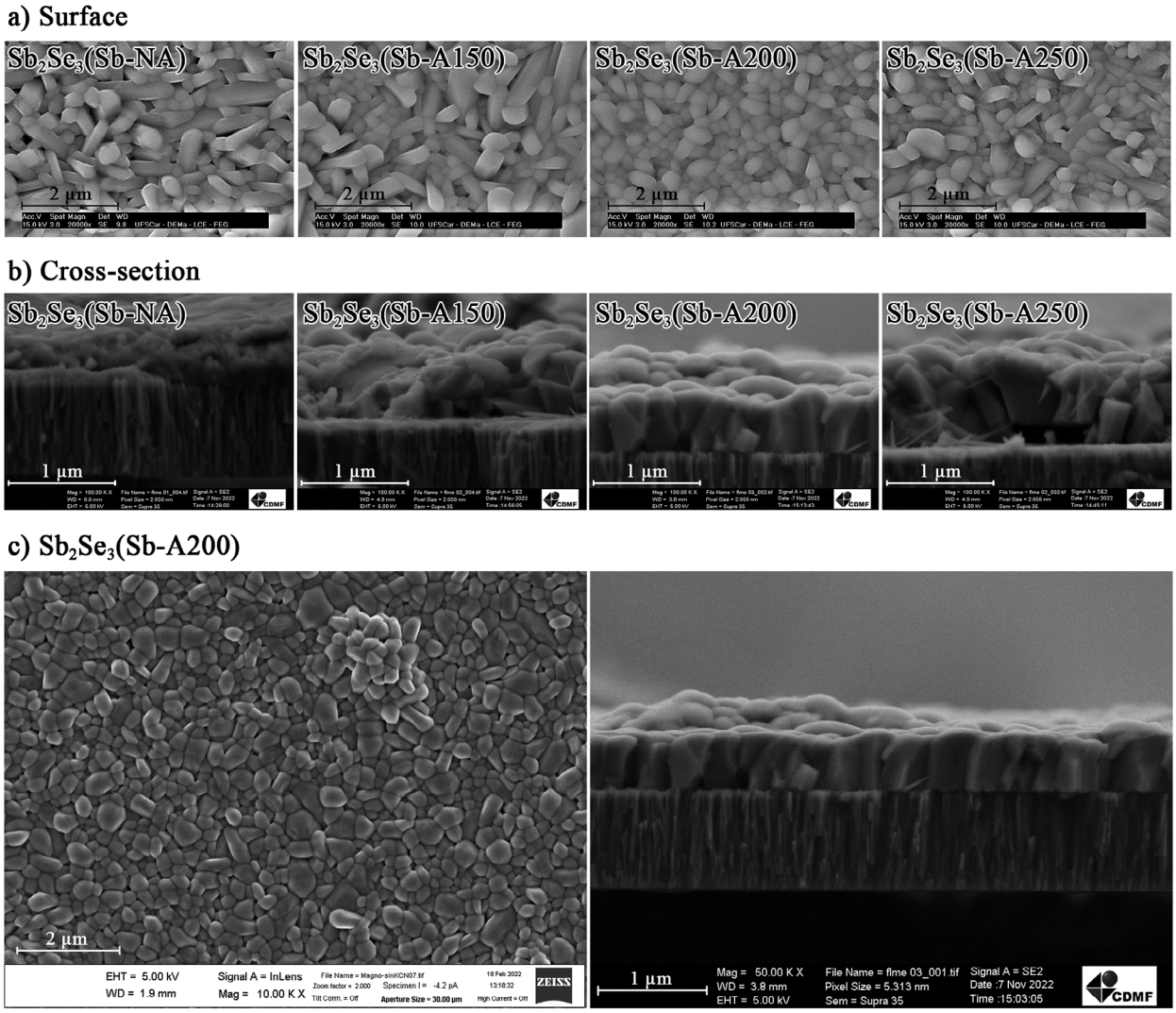


**Figure 4.** FEG-SEM micrographs of the a) surface (20k times magnification) and b) the cross-section (100k times magnification) for the $Sb_2Se_3$ (Sb-NA) and the $Sb_2Se_3$ (Sb-A) films. c) FEG-SEM micrographs zoomed out of the surface (10k times magnification) and cross-section (50k times magnification) of the $Sb_2Se_3$ (Sb-A200) film.

adjustment of the selenization temperature and time play an important role in improving the stoichiometry of the $Sb_2Se_3$ films.

Concerning the XRD analysis (Figure 5b), the diffraction peaks of all the samples were assigned to the orthorhombic $Sb_2Se_3$ phase (which follows the PDF no. 89–821), and no secondary phase, such as elemental Se and $Sb_2O_3$, was detected. Additionally, all the samples have shown strong reflections in the diffraction peak indexed to the (002) plane as the most intense one, indicating better crystallinity and preferential orientation of the $Sb_2Se_3$ crystal to the [001] direction. As additional analysis from the XRD patterns, it was also calculated the mean of crystallite size, $D$, from the diffraction peak positions via Equation (4)[65] for the $Sb_2Se_3$ (Sb-A200) films selenized at different temperatures and dwelling times.

$$D = \frac{K\lambda}{\beta \cos\theta} \tag{4}$$

where $K$ is the shape factor (0.9, considering the orthorhombic nature of $Sb_2Se_3$[65,66]), $\lambda$ is the X-ray wavelength (1.54 Å for Cu $K\alpha_1$ radiation), $\beta$ is the FWHM for a given diffraction peak, and $\theta$ is the diffraction peak position.

As shown in Figure 5c, a slight tendency was noted for the $D$ values of the samples selenized at different temperatures and dwelling times. For the dwelling time of 60 min, $D$ presented values ranging from 107.85 to 116.41 nm with increasing selenization temperature, suggesting an increase in the grain size as the temperature increases. This increase of $D$ may indicate that the crystallinity and grain size of the $Sb_2Se_3$ film are affected upon selenization. Since the film becomes Se-rich as the selenization temperature increases, the atoms of Se may incorporate into the $Sb_2Se_3$ structure[66] and increase its size. Conversely, for the dwelling time of 30 min, $D$ presented a maximum value of 112.61 nm for the selenization temperature of 300 °C and then this value decreased for higher selenization

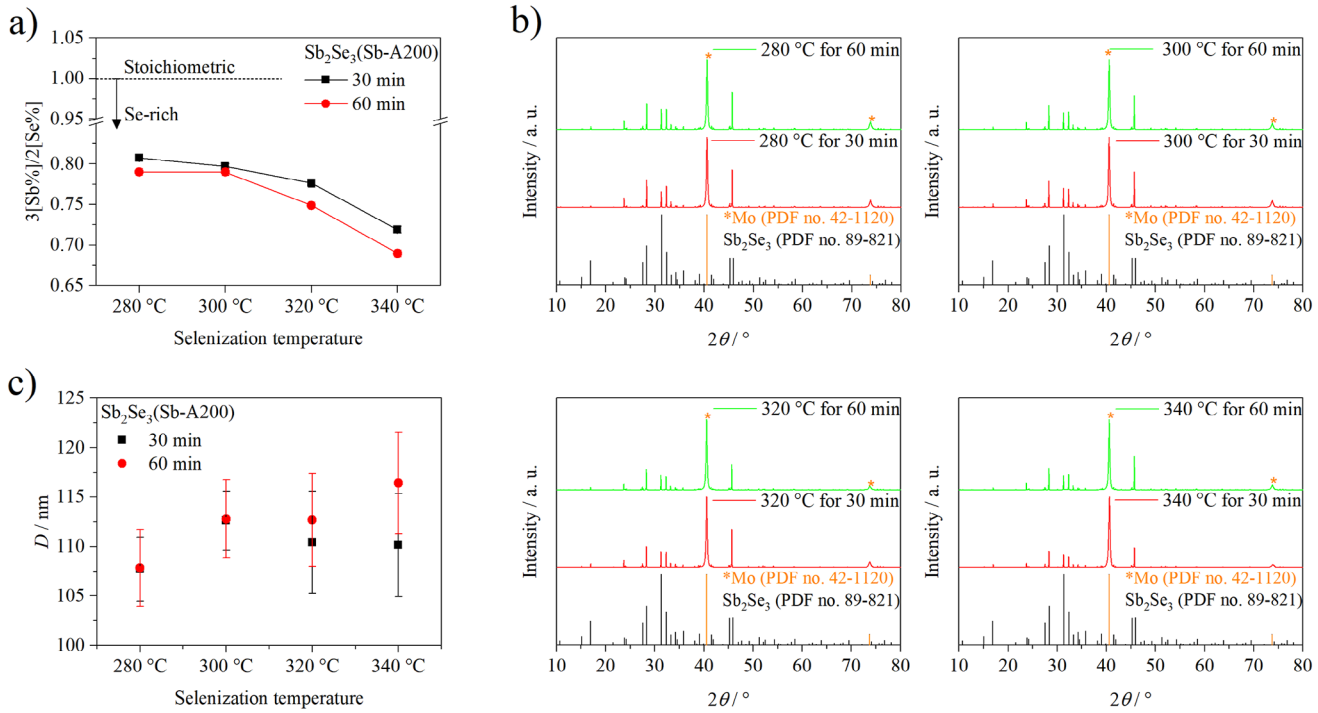


**Figure 5.** a) Atomic percentage ratio obtained from the XRF analysis, b) XRD patterns, and c) *D* values for the $Sb_2Se_3$(Sb-A200) films selenized at different temperatures and dwelling times. XRD patterns of the PDF database for the orthorhombic $Sb_2Se_3$ (PDF no. 89–821) and the cubic Mo (PDF no. 42–1120) phases are displayed as vertical lines at the bottom of the diffractograms. The diffraction peaks labeled with * were assigned to the Mo from the Mo back-contact.

temperatures. This decrease in the *D* values of the $Sb_2Se_3$ at selenization temperatures > 300 °C is probably related to the partial decomposition of the $Sb_2Se_3$ crystallites, as $Sb_2Se_3$ can undergo thermal decomposition and/or structural rearrangement under high temperatures.[47,67]

### 2.2. Characterization of Multi-Layered Films

Aiming to obtain a multilayer photocathode for the $H_2$ generation via solar-driven water splitting, the surface of the $Sb_2Se_3$(Sb-A200) film was initially etched with the KCN solution followed by the sequential deposition of the CdS and the $TiO_2$ layers onto their films' surface to obtain the $Sb_2Se_3$(Sb-A200)/CdS/$TiO_2$ films. Regarding the morphological analysis of the multilayer films, Figure S5 shows the surface micrographs obtained by FEG-SEM at 20k times magnification for each of the layers present in the sample. The surface of the back-contact (tri-layer Mo) presented a worm-like morphology, whereas the Sb-A200 layer, which was deposited onto this back-contact, exhibited a morphology of irregular grains closely packed. For the $Sb_2Se_3$(Sb-A200) film, obtained by selenizing the Sb-A200 film at 320 °C for 30 min, one notices that the particles featured irregular shape and once the $Sb_2Se_3$(Sb-A200) film was etched with the KCN solution, the irregular shape of the particles was drastically affected by the etching process, suggesting a slight dissolution of the particles of this layer.[18] For the CdS layer, which was deposited over the KCN-etched $Sb_2Se_3$(Sb-A200) film, it was noted the presence of vertically grown plate-like structures and the occurrence of clusters distributed throughout the CdS film's surface. For the upper layer, that is, $TiO_2$, one notices the presence of a compact layer covering the whole film's surface.

As additional SEM image analyses, it was also obtained the cross-section micrograph of the SLG/Mo/$Sb_2Se_3$(Sb-A200)/CdS/$TiO_2$ film to measure the thickness of the layers (**Figure 6a**). The tri-layer Mo exhibited a total thickness of ≈0.9 µm, which was comprised of the denominated $Mo_A$ (≈0.6 µm, lower region of the back-contact), and $Mo_B$ + $Mo_A$ (≈0.3 µm), corresponding to the porous (intermediate region of the Mo layer) and the sacrificial (upper region of the Mo layer) layers, respectively. It is worth mentioning that the difficulty in differentiating the porous and the sacrificial layers does not allow a proper distinction between them, however, the morphological characteristics of these layers are very similar to that reported in the literature.[68] It is also worth pointing out that the denomination of the layers in the tri-layer Mo (i.e., SLG/$Mo_A$/$Mo_B$/$Mo_A$) was based on the work developed by Lopez-Marino et al.,[68] who reported the tri-layer Mo was comprised of the $Mo_A$ layer (back-contact), deposited at high power and low pressure, $Mo_B$ (resistant to selenization), deposited at low power and high pressure, and the $Mo_A$ layer (sacrificial layer). The $Mo_A$ layer is more compact and has excellent electrical properties, but it is easily overselenized, whereas the $Mo_B$ layer is more porous and has higher shunt resistance. The presence of a thin $Mo_A$ layer on the upper region acts as a sacrificial layer for the formation of $MoSe_2$, and the interior selenization of the back-contact is prevented by the $Mo_B$ layer, leading thus the thick $Mo_A$ layer on the lower region unselenized, which acts as the back-contact for

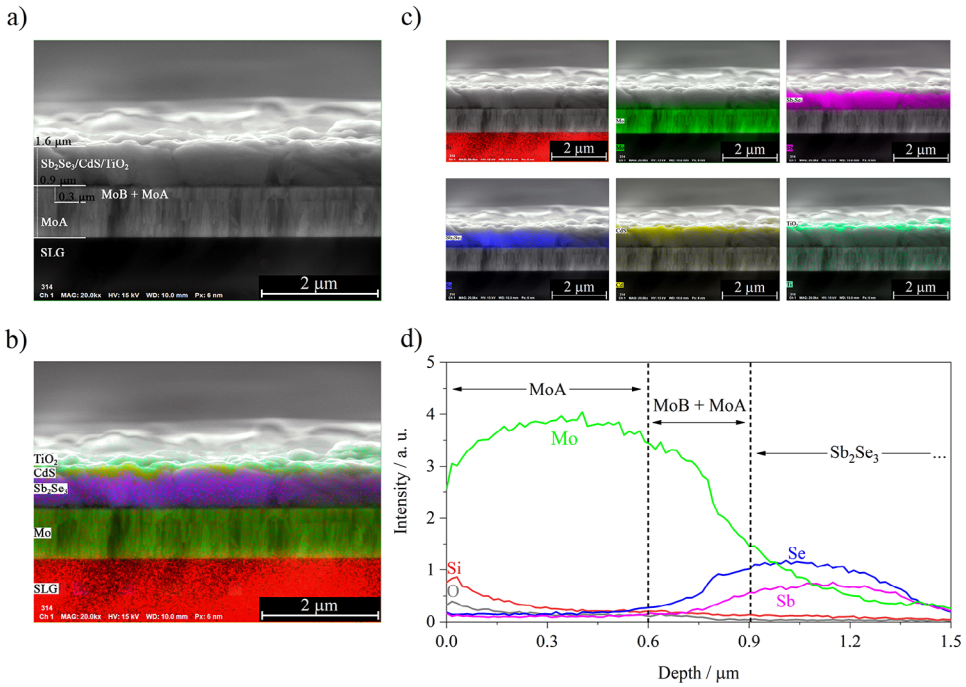


**Figure 6.** a) FEG-SEM cross-section micrograph (15k times magnification), b) EDS elemental mapping, and c) their respective elements for each layer present in the SLG/Mo/$Sb_2Se_3$(Sb-A200)/CdS/$TiO_2$ film. d) EDS scan line profile of the tri-layer Mo having on its surface the $Sb_2Se_3$(Sb-A200) film.

the light absorber material. Regarding the cross-section micrograph of the other materials deposited on the tri-layer Mo, one notices a very compact layer of the $Sb_2Se_3$(SbA200)/CdS/$TiO_2$ throughout the film's cross-section with a thickness of ≈0.7 µm, presenting no voids between the absorber and the tri-layer Mo and no apparent delamination. The XRF analysis was used to estimate the thickness of $Sb_2Se_3$, whose value is ≈0.65 µm, sufficient to absorb photons within the wavelength range of 400–1000 nm.[11,69] The CdS layer was estimated with a thickness of 50 nm, while $TiO_2$ was estimated with a thickness of ≈26 nm.

The cross-section of the multilayer film was also chemically characterized via EDS elemental mapping, it was possible to distinguish the elements in the different layers (see Figure 6b,c, and Figure S6a, Supporting Information). Additionally, according to the EDS scan line analysis (Figure 6d) along the cross-section of the film, one notices the presence of Se (blue line) located within 0.6 and 0.9 µm (roughly below the $Sb_2Se_3$ layer). That is due to the formation of a thick layer of $MoSe_2$ from the selenization of $Mo_B$ and $Mo_A$ (intermediate and upper region of Mo layer, respectively). The massive formation of $MoSe_2$ is prone to occur given that the molar Gibbs energies of the reaction of $MoSe_2$ and $Sb_2Se_3$ are both negative (Equations (5) and (6)), considering the reaction between $Mo_{(s)}$ or $Sb_{(s)}$ with $Se_{(g)}$ at 320 °C (corresponds to 593 K).[40,41] For more details about the calculation of the values of the $\Delta_r G$(593 K) for these reactions, the reader is referred to the SI. The presence of an $MoSe_2$ interlayer can improve the contact quality between the absorber (i.e., $Sb_2Se_3$) and the back contact by forming a quasi-ohmic contact, resulting in a higher open-circuit voltage due to a reduced contact barrier and minimized series resistance.[70]

Still concerning Figure 6d, it is noted that the presence of O (gray line) is located close to the lower region of the tri-layer Mo, and it is believed that this is from the glass substrate (i.e., $SiO_2$). Also, no O signal was identified within the region of the $Sb_2Se_3$(Sb-A200) film, which ensures the absence of $Sb_2O_3$ after the selenization process.

$$Mo_{(s)} + 2Se_{(g)} \rightarrow MoSe_{2(s)} \qquad \Delta_r G\ (593\ K) = -503.9\ kJ\ mol^{-1} \quad (5)$$

$$2Sb_{(s)} + 3Se_{(g)} \rightarrow Sb_2Se_{3(s)} \qquad \Delta_r G\ (593\ K) = -670.9\ kJ\ mol^{-1} \quad (6)$$

The remaining elements, such as Si, Cd, and Ti did not affect the $Sb_2Se_3$ layer, as can be seen in the EDS scan line complete analysis (Figure S6b, Supporting Information). Concerning the S element, it cannot be said how it affects the $Sb_2Se_3$ since Mo and S elements have small energy differences (14 eV) by energy dispersive X-ray, and it is hard to distinguish Mo and S elements with the energy resolution in EDS.[71] As long as the substrate is a thick layer of Mo (0 to 0.9 µm), it can be inferred that the huge signal in this range is related to the Mo element.

Additional chemical characterization was carried out for the $Sb_2Se_3$(Sb-A200)/CdS/$TiO_2$ film having on its surface deposited Pt, which was used as a cocatalyst to further improve the HER under illumination. The surface of the $Sb_2Se_3$(Sb-A200)/CdS/$TiO_2$/Pt film was assessed via EDS elemental mapping, as shown in Figure S6c, Supporting Information. The data verify the presence of Pt as well as Sb and Se, and these elements are well-distributed throughout the surface of the samples.

### 2.3. PEC Assessment

The PEC performance of the $Sb_2Se_3$(Sb-A200) films obtained from the selenization of Sb-A200 films at different

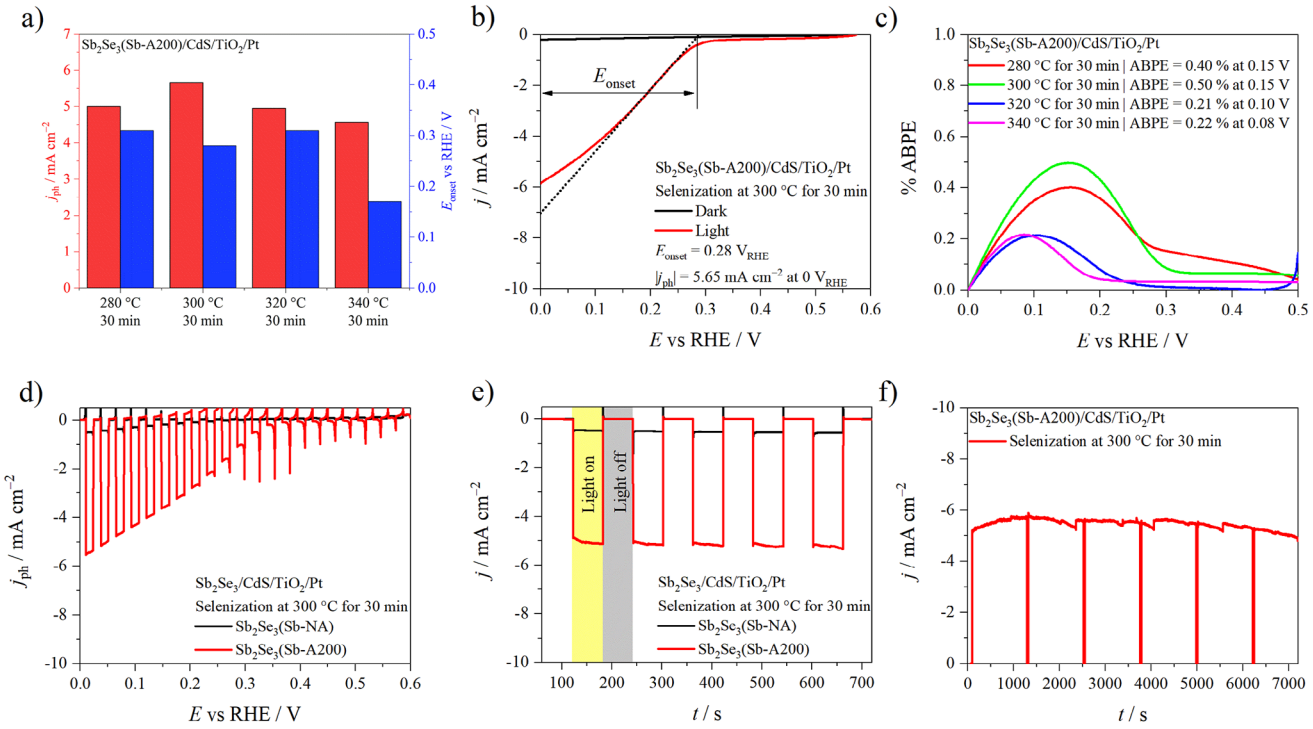


**Figure 7.** a) Summary of $j_{ph}$ at 0 $V_{RHE}$ and $E_{onset}$ values, b) LSVs (featuring $E_{onset}$ extrapolation) at a scan rate of 5 mV $s^{-1}$ in the dark and under solar illumination (100 mW $cm^{-2}$), c) ABPE plots, d) LSV measurement under chopped illumination (100 mW $cm^{-2}$), e) short-term stability, and f) long-term stability at 0 $V_{RHE}$ for the $Sb_2Se_3$(Sb-A200)/CdS/$TiO_2$/Pt films in different conditions. The electrolyte was a $N_2$-saturated solution of 0.5 mol $L^{-1}$ $H_2SO_4$ pH ≈ 0.3.

temperatures and dwelling times has been investigated. For this analysis, the selenized films were in a multilayer configuration, that is, $Sb_2Se_3$(Sb-A200)/CdS/$TiO_2$/Pt. The PEC experiments consisted of recording LSV curves in the dark and under solar illumination in a potential range between 0.6 $V_{RHE}$ and 0 $V_{RHE}$, as shown in Figure S7, Supporting Information.

For all the selenization conditions, the samples exhibited negative values of the current density, *j*, under illumination, as an indication of the cathodic current associated with the light-driven HER. This attribution is thermodynamically feasible, as the conduction band edge potential of the light absorber layer ($Sb_2Se_3$) is more negative than the potential of HER,[72] and that enables the transfer of the photogenerated electrons in the conduction band of the semiconductor to reduce $H_3O^+$ to produce $H_2$. From the LSV curves, one can obtain the photocurrent density, $j_{ph}$, by subtracting at a given potential the *j* under solar illumination from the *j* obtained in the dark (i.e., $j_{ph} = j_{light\ on} - j_{light\ off}$), and the $j_{ph}$ values at 0 $V_{RHE}$ are exhibited inside the graphs. As shown in Figure S7, Supporting Information, the different selenization temperatures did not significantly affect the $j_{ph}$ responses of the samples, however, the dwelling time had a considerable influence on the $j_{ph}$ values. The highest values of $j_{ph}$ at 0 $V_{RHE}$ were for the multilayer $Sb_2Se_3$(Sb-A200) films selenized for 30 min. The very low values of $j_{ph}$ for film selenized for 60 min are probably associated with the atomic ratio far from the stoichiometric condition.

In addition to the $j_{ph}$ analysis, it has also employed the LSV curves to assess the onset potential, $E_{onset}$, which is defined as the potential at which a specific reaction starts.[73] The $E_{onset}$ was estimated from the so-called tangent method, which consists of a linear extrapolation of the line tangent to the *j* curve (i.e., LSVs under illumination) until it intercepts the baseline,[73] wherein the interception corresponds to an approximate value of the $E_{onset}$. It is important to mention that the $E_{onset}$ obtained represented an estimated value to be used for making comparisons between the different samples in this work. For a more accurate determination of the $E_{onset}$ value, studies in literature recommend the use of mass-activity or specific-activity of a material,[73] however, this is out of the scope of this work. Regarding the estimated $E_{onset}$ from the LSVs (Figure S7, Supporting Information), for each selenization temperature, the $E_{onset}$ for the HER of the samples selenized for 30 min presented higher values than those selenized for 60 min. This result means that short selenization times can result in the obtainment of films with improved photoelectrocatalytic activity for the HER.

To ensure the reliability of the [001]-oriented $Sb_2Se_3$ film, LSVs were also performed on the $Sb_2Se_3$(Sb-A150) and $Sb_2Se_3$(Sb-A250) films in the same previous conditions, and the result can be assessed in the Figure S8, Supporting Information. It is possible to notice a huge improvement in both $j_{ph}$ and $E_{onset}$ of the $Sb_2Se_3$(Sb-A200) film when compared with the $Sb_2Se_3$(Sb-A150) and $Sb_2Se_3$(Sb-A250). These results are evidence that the Sb annealing before the selenization approach employed in this work can improve the performance of solar-driven water splitting.

To summarize the PEC assessment, **Figure** 7a displays the $j_{ph}$ and $E_{onset}$ values of the multilayer $Sb_2Se_3$(Sb-A200) films having the $Sb_2Se_3$ layer obtained from different selenization

temperatures for 30 min. The $j_{ph}$ values exhibited a slight trend as a function of the selenization temperature, and the maximum photoresponse for the HER was $j_{ph} = -5.65$ mA cm$^{-2}$ and $E_{onset} = 0.28$ $V_{RHE}$ for the selenization temperature of 300 °C (Figure 7b). Additional PEC analysis was conducted in terms of evaluating the efficiency of the PEC performance at the photocathode|electrolyte interface via ABPE. The highest value of ABPE was 0.50% at 0.15 $V_{RHE}$ for the multilayer $Sb_2Se_3$(Sb-A200) film obtained via selenization at 300 °C, whereas the ones selenized at 320 and 340 °C featured the lowest efficiencies, that is, 0.21% and 0.22%, respectively. Considering these results, the optimum selenization condition of the $Sb_2Se_3$(Sb-A200) films for PEC water splitting application is 300 °C for 30 min.

It was also made a comparison of the PEC performance of the $Sb_2Se_3$(Sb-A200) and $Sb_2Se_3$(Sb-NA) films, both selenized under the same conditions (i.e., 300 °C for 30 min), and these films also featured a multilayer configuration. For such, LSV measurements under chopped illumination were performed. The LSVs results (Figure 7d) show that the annealing step of the Sb film before selenization resulted in a huge increment of the $j_{ph}$ values for the HER, that is, the multilayer configuration featuring the $Sb_2Se_3$(Sb-A200) film presented a tenfold increase of the $j_{ph}$ at 0 $V_{RHE}$ compared to that of multilayer configuration having the $Sb_2Se_3$(Sb-NA) film. This increase of $j_{ph}$ is probably assigned to the preferential growth of the $Sb_2Se_3$ crystal to the [001] direction, which facilitates the transportation of the photogenerated carriers for the occurrence of the light-driven HER, and their stoichiometric characteristics compared to the $Sb_2Se_3$(Sb-NA) film. It is also important to make an attempt comparison of the PEC performance obtained in this work with the studies in literature, however, one should bear in mind that is rather difficult to make a fair/systematic comparison due to the different synthesis methods, power of the lamps used, and the variability of surface characteristics of the $Sb_2Se_3$ film (i.e., surface defects, dangling bonds, impurities, etc.). The results of $j_{ph}$ and $E_{onset}$ values described in this work are compared below to those reported in the literature,[74] nevertheless, the uniqueness of this work was the development of a simple and effective alternative method to improve the stoichiometry, crystallinity, and preferential orientation to the [001] direction of the $Sb_2Se_3$ film via employing the annealing of the Sb layer before their selenization.

In addition to the evaluation of the PEC activity, it has also assessed the short-term stability of both samples described previously. This experiment was performed by chronoamperometries, and the films were polarized at 0 $V_{RHE}$ for 10 min under chopped illumination (each light on and light off conditions spanned 60 s). As shown in Figure 7e, it was observed that a steady $j_{ph}$ with no noticeable decay during the time analyzed for both films, indicating good PEC stability for the light-driven HER. Additionally, the chronoamperometry measurements also displayed a tenfold increase of the $j_{ph}$ value for the multilayer configuration containing the $Sb_2Se_3$(Sb-A200) film compared to that of the $Sb_2Se_3$(Sb-NA) film, which follows the LSV measurements. This result confirms the efficacy of annealing of the Sb layer before selenization to improve PEC performance. It has also performed long-term stability measurement for the multilayer $Sb_2Se_3$(Sb-A200) film (Figure 7f), and one notices a stable $j_{ph}$ with a value of ≈−5 mA cm$^{-2}$ at 0 $V_{RHE}$ during 7000 s, suggesting thus no noticeable photocorrosion of the films during the light-driven HER.

### 2.4. Efficiency Analysis

Since there was a huge difference in the PEC performance between the multilayer configuration having the $Sb_2Se_3$(Sb-A200) and the $Sb_2Se_3$(Sb-NA) films, efficiency analysis was employed to better understand the main loss mechanism occurring in both samples. The reader is referred to SI for details about the calculation of the efficiency analysis. Based on the integration of the curve in **Figure 8a** by employing Equation S8, Supporting Information, it was obtained a maximum photocurrent density, $j_{ph,max}$, for the $Sb_2Se_3$ semiconductor of 39.9 mA cm$^{-2}$ (for its corresponding $E_g$ of 1.2 eV), as reported in the literature.[27] Conversely, the absorption photocurrent density, $j_{ph,abs}$, was calculated from the employment of Equation S15, Supporting Information, and is displayed in Figure 8b. It notices $j_{ph,abs}$ values of 29.8 and 27.1 mA cm$^{-2}$ for the $Sb_2Se_3$(Sb-A200) and the $Sb_2Se_3$(Sb-NA) films, respectively. These results did not represent significative differences between them for these films, and this is due to the $E_g$ values being very similar to both films. This means that the decrease in the PEC performance of the $Sb_2Se_3$(Sb-NA) film compared to that of the $Sb_2Se_3$(Sb-A200) film is not due to loss of light absorption in the $Sb_2Se_3$.

As additional analyses to determine the nature of the limiting factor(s) for the PEC performance of the films, the transfer ($\eta_{transf.}$) and separation ($\eta_{sep.}$) efficiencies were calculated from the Equations (7) and (8),[75–77] and the results are shown in Figure 8c,d. For this analysis, it was used as an electron scavenger,[78] a solution of 0.5 mol L$^{-1}$ $Na_2S_2O_8$ dissolved in the electrolyte.

$$\eta_{trasnf.} = \frac{j_{ph}}{j_{ph(Na_2S_2O_8)}} \quad (7)$$

$$\eta_{sep.} = \frac{j_{ph(Na_2S_2O_8)}}{j_{ph,abs}} \quad (8)$$

The $\eta_{transf.}$ of the $Sb_2Se_3$(Sb-A200) and $Sb_2Se_3$(Sb-NA) films did not provide a relevant difference between their values (57% and 43% at 0 $V_{RHE}$, respectively), whereas the $\eta_{sep.}$ of these films differed drastically in 29% (i.e., 33% and 4% at 0 $V_{RHE}$, respectively). Bearing in mind that the $\eta_{sep.}$ represents the fraction of minority charge carriers reaching the surface of the semiconductor, while the remaining carriers recombine in the bulk.[79] Although the $j_{ph,abs}$ of the $Sb_2Se_3$(Sb-A200) and the $Sb_2Se_3$(Sb-NA) films did not significantly change, the $\eta_{sep.}$ values suggest that a significant portion of the photogenerated charge carriers in the $Sb_2Se_3$(Sb-NA) film undergo recombination before reaching the surface of the photoelectrode. In other words, the influence of annealing of Sb film before its selenization not only improved the crystallinity and preferential orientation to the [001] direction and stoichiometry but also directly resulted in a decrease in bulk recombination of the electron-hole pairs. Overall, these factors mentioned above featured a substantial improvement in the PEC performance toward light-driven HER due to the annealed Sb films submitted to selenization.

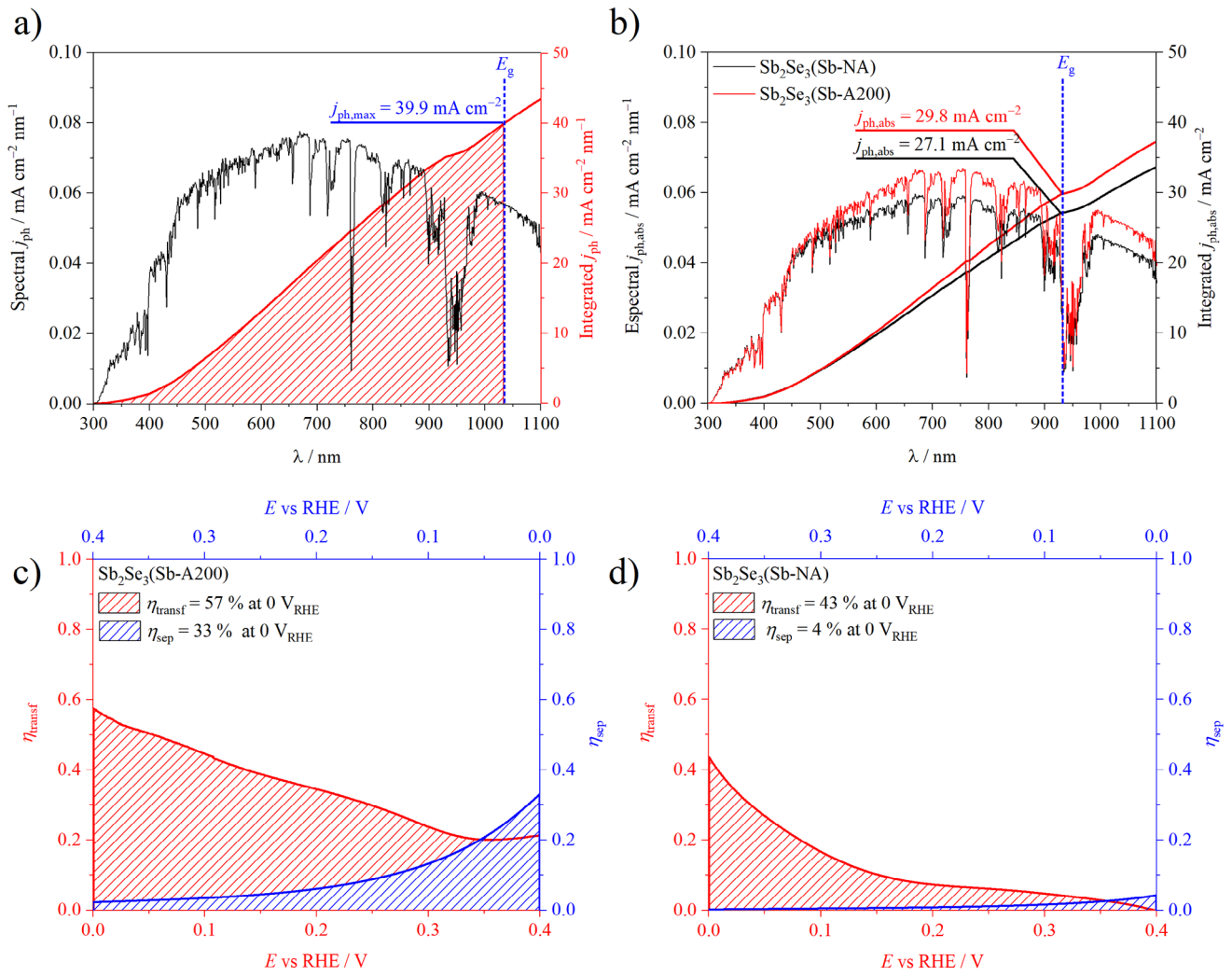


**Figure 8.** a) $j_{ph,max}$ for ideal $Sb_2Se_3$ semiconductor and b) $j_{ph,abs}$ for the $Sb_2Se_3$ films. $\eta_{transf.}$ and $\eta_{sep.}$ for c) the $Sb_2Se_3$ (Sb-A200) and d) the $Sb_2Se_3$ (Sb-NA) films. The electrolyte was a $N_2$-saturated solution of 0.5 mol $L^{-1}$ $H_2SO_4$ pH ≈ 0.3 + 0.5 mol $L^{-1}$ $Na_2S_2O_8$.

## 3. Conclusions

In the final analysis, the employment of an annealing step of the Sb film before selenization is utterly important to obtain $Sb_2Se_3$ film featuring high crystallinity, suitable stoichiometry, and preferential [001] orientation, which is required to favor charge carrier transportation to ultimately boost PEC $H_2$ generation. The crystal orientation was assessed by the TC(*hkl*) calculated from the XRD data, which showed TC(002) ≫ 1 for the optimized condition, indicating that the annealing of the Sb film favored the formation of highly oriented $Sb_2Se_3$ crystals in the [001] direction during the selenization step. Annealing the Sb film resulted in the formation of Sb film crystallographically oriented to the [001] direction, which might have ultimately contributed to obtaining [001]-oriented $Sb_2Se_3$ during the selenization process. The $Sb_2Se_3$ film obtained only by selenizing the non-annealed Sb film displayed TC(230) > 1, meaning that the $Sb_2Se_3$ crystal is oriented to the [*hk*0] direction, which hinders charge carriers' transportation. The Sb annealing approach was also beneficial for improving the crystallinity degree and the atomic ratio of the $Sb_2Se_3$ films as verified by the XRD and XRF analyses, respectively. In terms of PEC performance for the HER, the $Sb_2Se_3$(Sb-A200)/CdS/$TiO_2$/Pt film resulted in delivering a considerable $j_{ph}$ = −5.65 mA cm$^{-2}$ at 0 $V_{RHE}$, representing a tenfold increase compared to that of the $Sb_2Se_3$(Sb-NA)/CdS/$TiO_2$/Pt film. The $Sb_2Se_3$ film synthesized from the optimized condition also displayed stable photoelectroresponse for the HER over 7000 s of continuous experiment, and a higher value of efficiency for the photogenerated charge carriers' separation. Based on all these results, the improved PEC performance of the $Sb_2Se_3$ film, obtained from selenization of the annealed Sb, was due to the preferred $Sb_2Se_3$ crystal growth in [001] direction, improvement of crystallinity and stoichiometry, and reduced occurrence of the electron-hole recombination process. Last, this work contributes with an alternative approach to obtain [001]-oriented $Sb_2Se_3$ film and paves the way for future studies to further modify this material to

achieve even higher PEC activity for $H_2$ generation via water splitting.

## 4. Experimental Section

*Fabrication of SLG/Mo Substrate*: Soda-lime glass (SLG) plates, with dimensions of 2 cm × 2 cm, were cleaned with glassware detergent and then ultrasonicated with acetone, isopropanol, and deionized water for 10 min in each solvent, followed by drying with argon (Ar) gas. Subsequently, the SLG plates were coated with a tri-layer structure of molybdenum (Mo) with ≈900 nm of thickness by employing a DC-magnetron sputtering (Alliance Concept AC450) and used as substrate (SLG/Mo, where the metal acts as back-contact) for the deposition of the $Sb_2Se_3$ film.[80] Each of the tri-layer Mo configurations was obtained at different sputtering deposition conditions, that is, power and pressure, which are described somewhere else.[68] The tri-layer Mo configuration has been employed in this way to minimize its overselenization (formation of a thick layer of $MoSe_2$) during the thermal treatment process, which could be detrimental to the performance of the solar energy conversion devices. Additionally, the tri-layer Mo deposited on the SLG has been used to improve efficiency and enhance the performance of photovoltaic devices.[68] The SLG/Mo was omitted in the sample labels (presented in the following section) and will be indicated when it is essential for the discussion of the results.

*Synthesis of $Sb_2Se_3$ Film*: The Sb layer (thickness of ≈250 nm) was deposited on the substrate via thermal evaporation (MBraun MBEvap) using Sb beads as the material source (Sigma-Aldrich 99.999%) placed on a Mo boat. The pressure of the system was set at $1 \times 10^{-5}$ mbar, the deposition rate was ≈10 Å $s^{-1}$, and the holder rotation was 5.5 RPM.[37] The as-deposited Sb layer on the substrate was subjected afterward to the annealing process in a three-zone tube furnace (Nabertherm). For the thermal treatment experiment, four approaches were investigated: a) selenization of non-annealed Sb, b) annealing temperature effect of Sb, c) selenization of annealed Sb at different temperatures, and d) optimizing selenization of annealed Sb. The first approach consisted of selenizing the non-annealed Sb film at 320 °C for 30 min (labeled as $Sb_2Se_3$ (Sb-NA)). The second one concerned the annealing temperature effect of the Sb films without selenization, which were annealed at 150, 200, and 250 °C for 30 min, and the samples were labeled as Sb-A150, Sb-A200, and Sb-A250, respectively, or Sb-A as a general label. The third approach consisted of selenizing the annealed Sb films in the same previous conditions, that is, the as-deposited Sb films were annealed at different temperatures, namely, 150, 200, and 250 °C for 30 min, followed by selenization at 320 °C for 30 min and the samples were labeled as $Sb_2Se_3$ (Sb-A150), $Sb_2Se_3$ (Sb-A200), and $Sb_2Se_3$ (Sb-A250), respectively, or $Sb_2Se_3$ (Sb-A) as a general label. The fourth approach encompassed the optimization of the selenization temperatures (i.e., 280, 300, 320, and 340 °C) and times (i.e., 30 and 60 min) for the annealed Sb. The sample was placed in a Petri dish inside the three-zone tube furnace and then submitted to an inert Ar atmosphere (internal pressure of 500 mbar). For the selenization experiments, 10 mg of Se powder (ThermoScientific) was placed inside the Petri dish. For all the approaches, the thermal treatment was performed under an Ar atmosphere and employed a heating rate of 10 °C $min^{-1}$; the cooling process was done naturally to room temperature. These thermal treatment approaches developed in this work are summarized in Figure S1, Supporting Information for a better overview.

*Etching with KCN*: The samples thermally treated were subsequently placed facing up in a Petri dish filled with a 2% m/v KCN solution for the etching process. The samples were etched for 40 min at room temperature and then washed extensively with ultrapure water (Milli-Q) and dried with $N_2$.[18] According to the literature, KCN etching has been widely used in photovoltaic absorbers, such as CZTS,[81] CIGSSe,[82] CZTSSe,[83] and $Sb_2Se_3$,[18] as it has a positive impact on the electronic structure and superficial chemical composition of these materials. According to Jiménez-Guerra et al., etching $Sb_2Se_3$ film with KCN solution produces very Sb-rich surfaces, without affecting the bulk property, and inverts $Sb_2Se_3$'s polarity, creating thus a buried junction with CdS, which improves the fill factor of the photovoltaic device.[18]

*Deposition of CdS Film*: CdS film, which is an n-type semiconductor commonly used as an electron transport layer,[84] was immediately deposited on the KCN-modified $Sb_2Se_3$ film by chemical bath deposition to form the $Sb_2Se_3$/CdS heterostructure. This aimed to protect $Sb_2Se_3$ films from any formation of superficial oxides as well as to further improve PEC performance. For this experiment, it was employed a total volume of 200 mL of CdS bath solution, which the preparation consisted of heating 100 mL of ultrapure water to 75 °C and then sequentially adding 55 mL of 0.1 mol $L^{-1}$ $Cd(NO_3)_2$, 30 mL of 1 mol $L^{-1}$ $Na_3C_6H_5O_7$, and 5 mL of $NH_4OH$ (adapted from Vigil-Galán et al.[85]). The samples were affixed onto a 4 cm × 4 cm plate glass using Kapton tape and placed vertically on a PTFE support. This system was immersed in the CdS bath solution and waited ≈5 min for stabilization, followed by the addition of 10 mL of 1 mol $L^{-1}$ $(NH_2)_2CS$. At this point, the chemical bath solution was kept under continuous stirring for 40 min, which was the deposition time. After that, the samples were removed from the bath, exhaustively rinsed with ultrapure water, and dried with Ar gas.

*Deposition of $TiO_2$ Film*: Aiming to protect the $Sb_2Se_3$/CdS heterojunction against photocorrosion, a protective layer of $TiO_2$ was deposited, which is a stable material even in aqueous media.[86] The layer was deposited over the $Sb_2Se_3$/CdS film by the thermal atomic layer deposition (ALD, Veeco Savannah 200) technique. The samples were heated at 175 °C, and the deposition was performed using tetrakis(dimethylamino)titanium(IV) (TDMAT) as Ti precursor source and $H_2O$ as an oxidant agent. The TDMAT precursor was heated at 75 °C during the deposition process, and the $H_2O$ cylinder was set at room temperature. It employed 600 cycles for the deposition of the $TiO_2$ layer, and each cycle corresponded to exposing the samples to the TDMAT for 0.1 s followed by a 10 s purge of $N_2$, and then exposing the samples to $H_2O$ vapor for 0.02 s with a subsequent purge with $N_2$ for 10 s. The growth rate of the $TiO_2$ film was 0.43 Å/cycle, resulting in a layer with a thickness of ≈26 nm.

*Processing Photoelectrodes for PEC Measurements*: To avoid losses of photoresponse signal of the photoelectrodes during the PEC measurements, it is utterly important to ensure a good electrical contact in the region where the connector is clipped onto the photoelectrode's back-contact. In this sense, an indium-based (In-based) solder was used to deposit a melted In layer on the upper region of the substrate (Figure S2a, Supporting Information). Then, the edges of the $Sb_2Se_3$/CdS/$TiO_2$ layers were properly removed to minimize potential border defects and to circumvent shunt resistance issues.[87] Subsequently, a highly chemically stable and electrically insulating epoxy resin was used to cover the exposed edges of the Mo film (Figure S2a,b, Supporting Information), which cannot be in contact with the supporting electrolyte during the PEC measurements. The epoxy resin was allowed to dry for 24 h to ensure complete removal of the dispersing solvent from the polymer. The films' geometrical area delimited by the epoxy resin was determined from their photographs, which were taken close to a caliper, and using the ImageJ software.[88] The geometrical area of the films was typically in the range of 0.1 – 0.2 $cm^2$.

*Photoelectrodeposition of Pt Nanoparticles*: Since Pt is highly electrocatalytic for the HER and can easily transfer electrons at the photoelectrode|electrolyte interface,[89] it was photoelectrodeposited Pt nanoparticles over the film surface to further boost the HER. As a Pt precursor source, it was employed a solution containing 1.0 mmol $L^{-1}$ $H_2PtCl_6 \cdot xH_2O$ in 0.1 mol $L^{-1}$ phosphate-buffered solution (PBS) at pH 6.5 and 0.1 mol $L^{-1}$ $Na_2SO_4$ (Sigma-Aldrich), which was previously deaerated for 15 min with $N_2$ flow before the Pt deposition on the samples. Pt photoelectrodeposition was carried out in a three-electrode cell with a quartz window and using a potentiostat/galvanostat (BioLogic VSP). The counter electrode was a Pt plate with a geometric area of ≈1 $cm^2$, while the reference electrode was an $Ag/AgCl/Cl^-_{(sat.\ KCl)}$, that is, all the potential values presented in the text are referenced against the $Ag/AgCl/Cl^-_{(sat.\ KCl)}$ electrode, unless the reversible hydrogen electrode (RHE) is specified. The working electrode was the $Sb_2Se_3$/CdS/$TiO_2$ film. The Pt deposition was performed in galvanostatic mode, applying a current density of –0.05 mA $cm^{-2}$ for 10 min, and under a solar light simulator (Newport LSH-7320

LED, 100 mW cm$^{-2}$).[90] Figure S2c, Supporting Information summarizes all the steps involved in the fabrication of the complete device, which will be employed as photoelectrode for the PEC measurements.

*Physical and Chemical Characterization*: The crystalline structure of the $Sb_2Se_3$ was characterized by X-ray powder diffraction (XRD, Bruker D8 Advance) with Cu $K\alpha_1$ radiation of 1.54 Å and a scan rate of 0.02° s$^{-1}$ in a $2\theta$ range between 10 and 80°. The vibrational modes of $Sb_2Se_3$ were investigated by Raman spectroscopy (Renishaw Raman microscope) under a 532 nm excitation laser. Morphological characterization and cross-section measurements were performed via high-resolution field emission scanning electron microscopy (FE-SEM, Neon40 Crossbeam, and Philips XL-30 FEG) operating with 15 kV and using an in-lens detector. The chemical composition was assessed employing X-ray fluorescence (XRF, Fischerscope X-ray). The elemental mapping of the top surface and cross-section of the samples was carried out on a FE-SEM (Jeol JSM-7200F) equipped with an energy-dispersive X-ray spectrometer (EDS, Bruker XFlash 6|60 detector). It was also evaluated the superficial chemical composition of the $Sb_2Se_3$ film via X-ray photoelectron spectroscopy (XPS, Scienta Omicron ESCA 2SR) with Al $K\alpha_1$ radiation (1486.7 eV), which was the excitation source. All the XPS spectra were adjusted by setting the C 1s peak at 284.5 eV and employing the Gaussian-Lorentzian function (30%) for the peak adjustment and the Tougaard function for the background. The XPS spectra processing was done with the CasaXPS software.[91] The optical $E_g$ was estimated from the diffuse reflectance spectra recorded on a UV–vis-NIR spectrophotometer (Cary 5E) and calculated via Kubelka-Munk function, $f(R)$, and Tauc plots (Equations (9) and (10)[92,93]).

$$f\ (R) = \frac{a}{s} = \frac{(1-R)^2}{2R} \tag{9}$$

$$(ah\nu)^n = A_0\ \left(h\nu - E_g\right) \tag{10}$$

where $s$ is the scattering coefficient, which was considered to be wavelength independent and that means that $f(R)$ can be used instead of $a$,[51] $R$ is the absolute diffuse reflectance, $h$ is the Planck constant (6.626 × 10$^{-34}$ J s), $n$ assumes the values of 2 or 2/3 for direct transition (allowed and forbidden, respectively) and 1/2 or 1/3 for indirect transition (allowed and forbidden, respectively), $A_0$ is a constant, and $\nu$ is the frequency of radiation.

Urbach energy, $E_u$, which describes the occurrence of band tail energy within the $E_g$,[56] was calculated from Equation (11):[94]

$$a = a_0 \exp\left(\frac{E_{ph}}{E_u}\right) \tag{11}$$

where the $a_0$ is a constant and $E_{ph}$ is the photon energy, and such is defined in Equation (12):

$$E_{ph} = h\nu \tag{12}$$

The values of $E_u$ can be determined from the inverse of the slope in the linear region (below the optical $E_g$) of the ln $a$ versus $E_{ph}$ graphs.

*Photoelectrochemical Characterization*: The PEC experiments were carried out in the same cell configuration and solar simulator as described previously. The supporting electrolyte was a solution containing 0.5 mol L$^{-1}$ $H_2SO_4$ pH ≈ 0.3 (measured pH), and this solution was deaerated with $N_2$ flow for 15 min before the PEC experiments. To evaluate the PEC activity for the $H_2$ generation, it was employed linear sweep voltammetry (LSV) in the dark and under illumination, as well as under chopped illumination. The LSVs were recorded at a scan rate of 5 mV s$^{-1}$ and were scanned from the open-circuit potential to the thermodynamic potential of the HER at pH 0.3. The potential values recorded against the Ag/AgCl/Cl$^-_{(sat.\ KCl)}$ electrode were converted to potential values relative to the RHE by using Equation (13).[95,75,76]

$$E\ (\text{versus RHE}) = E_{appl.}\left(\text{versus Ag/AgCl/Cl}^-_{(sat.\ KCl)}\right) + \text{pH}\ \times 0.059 + 0.197 \tag{13}$$

Chronoamperometry measurements were employed to check the short-term stability of the samples, and this experiment was conducted by polarizing the samples at 0 $V_{RHE}$ for 660 s under chopped illumination (pulses of 60 s for each light on and light off conditions (Thorlabs SHB1T diaphragm shutter)). It was also performed long-term stability tests for 2 h under chopped illumination (pulsed light, alternating 20 min of light on and 30 s of light off) for the samples polarized at 0 $V_{RHE}$. The current values, obtained from the LSVs and chronoamperometries, were normalized by the geometric area. The geometric area was obtained from the photograph processing of the photoelectrodes, as described previously. The applied bias photon-to-current efficiency (ABPE) of the photocathodes was calculated from Equation (14).[51] It is worth noting that the PEC experiments performed to obtain this efficiency were conducted in a three-electrode cell configuration (i.e., bias was applied between the working and reference electrodes). This means that the ABPE values obtained in this work represent the efficiency of the PEC performance at the photocathode|electrolyte interface and not the efficiency of an entire PEC device.[51] Despite this, the ABPE results are valuable in providing insights about the semiconductor material and its interface properties.

$$\text{ABPE}\ = \left[\frac{\left|j_{ph}\right|\left[E_{appl.}\ (\text{versus RHE}) - 0\right]\eta_F}{I}\right]_{AM1.5G} \tag{14}$$

where $E_{appl.}$(versus RHE) is the applied potential relative to the RHE, $j_{ph}$ is the photocurrent density at a given $E_{appl.}$ (versus RHE) value, which was obtained from the LSVs, $\eta_F$ is the faradaic efficiency (considered 100% for this study), and $I$ is the solar simulator irradiance on the photocathode (100 mW cm$^{-2}$).

## Supporting Information

Supporting Information is available from the Wiley Online Library or from the author.

## Acknowledgements

This study was financed, in part, by the São Paulo Research Foundation (FAPESP), Brazil. Process numbers #2021/07727-0, #2017/21365-8, #2017/11986-5, #2016/12681-0, #2013/07296-2; the Conselho Nacional de Desenvolvimento Científico e Tecnológico (*CNPq*) [grant numbers #406156/2022-0 and #311769/2022-5]; FINEP-MCTI 01.22.0179.00, the European Union H2020 Framework Programme under Grant Agreement No. 866018, Low dimensional semiconductors for optically tuneable solar harvesters (SENSATE); the Spanish Ministry of Science and Innovation under the MATER-ONE project (PID2020-116719RB-C41 and C44), MIRACLE project (TED2021-130265B-C21) and INTELEC project (TED2021-130461B-I00). E.S. acknowledges the ICREA Academia program. The authors also would like to thank Prof. Dr. Valmor R. Mastelaro from Universidade de São Paulo (USP) for obtaining the XPS spectra of the samples.

The Article Processing Charge for the publication of this research was funded by the Coordenação de Aperfeiçoamento de Pessoal de Nível Superior - Brasil (CAPES) (ROR identifier: 00x0ma614).

## Conflict of Interest

The authors declare no conflict of interest.

## Data Availability Statement

The data that support the findings of this study are available from the corresponding author upon reasonable request.

## Keywords

hydrogen, photoelectrochemical water splitting, preferential orientation, $Sb_2Se_3$, solar energy

Received: March 11, 2025
Revised: March 21, 2025
Published online:

[1] L. M. Peter, K. G. U. Wijayantha, *ChemPhysChem* **2014**, *15*, 1983.
[2] J. F. Brito, A. A. Silva, A. J. Cavalheiro, M. V. B. Zanoni, *Int. J. Electrochem. Sci.* **2014**, *9*, 5961.
[3] F. M. Guangul, G. T. Chala, In *2019 4th MEC International Conference on Big Data and Smart City (ICBDSC)*, IEEE, Muscat, **2019**, pp. 1–5.
[4] C. Jiang, S. J. A. Moniz, A. Wang, T. Zhang, J. Tang, *Chem. Soc. Rev.* **2017**, *46*, 4645.
[5] M. Rashad, M. Daowd, A. M. A. Amin, *Recent Adv. Environ. Earth Sci. Econ.* **2015**, 167.
[6] T. R. Cook, D. K. Dogutan, S. Y. Reece, Y. Surendranath, T. S. Teets, D. G. Nocera, *Chem. Rev.* **2010**, *110*, 6474.
[7] D. Merki, H. Vrubel, L. Rovelli, S. Fierro, X. Hu, Fe, Co, *Chem. Sci.* **2012**, *3*, 2515.
[8] M. R. A. Bhuiyan, *Micro Nano Lett.* **2022**, *17*, 402.
[9] J. Tan, W. Yang, Y. Oh, H. Lee, J. Park, J. Moon, *ACS Appl. Mater. Interfaces* **2018**, *10*, 10898.
[10] K. Zeng, D.-J. Xue, J. Tang, *Semicond. Sci. Technol.* **2016**, *31*, 063001.
[11] C. Chen, W. Li, Y. Zhou, C. Chen, M. Luo, X. Liu, K. Zeng, B. Yang, C. Zhang, J. Han, J. Tang, *Appl. Phys. Lett.* **2015**, *107*, 043905.
[12] C. E. Patrick, F. Giustino, *Adv. Funct. Mater.* **2011**, *21*, 4663.
[13] L. Zhang, Y. Li, C. Li, Q. Chen, Z. Zhen, X. Jiang, M. Zhong, F. Zhang, H. Zhu, *ACS Nano* **2017**, *11*, 12753.
[14] X. Liu, J. Chen, M. Luo, M. Leng, Z. Xia, Y. Zhou, S. Qin, D. Xue, L. Lv, H. Huang, D. Niu, J. Tang, *ACS Appl. Mater. Interfaces* **2014**, *6*, 10687.
[15] L. Wang, D.-B. Li, K. Li, C. Chen, H.-X. Deng, L. Gao, Y. Zhao, F. Jiang, L. Li, F. Huang, Y. He, H. Song, G. Niu, J. Tang, *Nat. Energy* **2017**, *2*, 17046.
[16] U. Wijesinghe, G. Longo, O. S. Hutter, *Energy Adv.* **2023**, *2*, 12.
[17] S. Chen, T. Liu, M. Chen, M. Ishaq, R. Tang, Z. Zheng, Z. Su, X. Li, X. Qiao, P. Fan, G. Liang, *Nano Energy* **2022**, *99*, 107417.
[18] M. Jiménez-Guerra, L. Calvo-Barrio, J. M. Asensi, I. Caño-Prades, S. Yan, E. Barrena, J. Puigdollers, Z. Jehl, Y. Sánchez, E. Saucedo, *ACS Appl. Energy Mater.* **2024**, *7*, 874.
[19] Y. Zhou, M. Leng, Z. Xia, J. Zhong, H. Song, X. Liu, B. Yang, J. Zhang, J. Chen, K. Zhou, J. Han, Y. Cheng, J. Tang, *Adv. Energy Mater.* **2014**, *4*, 1301846.
[20] Y. Zhou, L. Wang, S. Chen, S. Qin, X. Liu, J. Chen, D.-J. Xue, M. Luo, Y. Cao, Y. Cheng, E. H. Sargent, J. Tang, *Nat. Photonics* **2015**, *9*, 409.
[21] M. B. Costa, F. W. de Souza Lucas, L. H. Mascaro, *ChemElectroChem* **2017**, *4*, 2507.
[22] C. Chen, D. C. Bobela, Y. Yang, S. Lu, K. Zeng, C. Ge, B. Yang, L. Gao, Y. Zhao, M. C. Beard, J. Tang, *Front. Optoelectron.* **2017**, *10*, 18.
[23] K. U. Isah, J. A. Yabagi, U. Ahmadu, M. I. Kimpa, M. G. Z. Kana, A. A. Oberafo, *IOSR-JAP* **2013**, *2*, 14.
[24] I. L. Validžić, M. Mitrić, N. D. Abazović, B. M. Jokić, A. S. Milošević, Z. S. Popović, F. R. Vukajlović, *Semicond. Sci. Technol.* **2014**, *29*, 035007.
[25] B. Yang, L. Wang, J. Han, Y. Zhou, H. Song, S. Chen, J. Zhong, L. Lv, D. Niu, J. Tang, *Chem. Mater.* **2014**, *26*, 3135.
[26] W. Yang, J. Park, H.-C. Kwon, O. S. Hutter, L. J. Phillips, J. Tan, H. Lee, J. Lee, S. D. Tilley, J. D. Major, J. Moon, *Energy Environ. Sci.* **2020**, *13*, 4362.
[27] W. Yang, J. H. Kim, O. S. Hutter, L. J. Phillips, J. Tan, J. Park, H. Lee, J. D. Major, J. S. Lee, J. Moon, *Nat. Commun.* **2020**, *11*, 861.
[28] M. B. Costa, F. W. de Souza Lucas, L. H. Mascaro, *J. Solid State Electrochem.* **2018**, *22*, 1557.
[29] P. Prajapat, P. Vashishtha, P. Goswami, G. Gupta, *Mater. Sci. Semicond. Process.* **2024**, *169*, 107873.
[30] P. Li, X. Yuan, M. Feng, F. Ran, D. Zhang, S. Chen, *Appl. Phys. Lett.* **2021**, *119*, 102101.
[31] I. Caño, P. Vidal-Fuentes, L. Calvo-Barrio, X. Alcobé, J. M. Asensi, S. Giraldo, Y. Sánchez, Z. Jehl, M. Placidi, J. Puigdollers, V. Izquierdo-Roca, E. Saucedo, *ACS Appl. Mater. Interfaces* **2022**, *14*, 11222.
[32] W. Lian, R. Cao, G. Li, H. Cai, Z. Cai, R. Tang, C. Zhu, S. Yang, T. Chen, *Adv. Sci.* **2022**, *9*, e2105268.
[33] J. Otavio Mendes, A. Merenda, K. Wilson, A. Fraser Lee, E. Della Gaspera, J. van Embden, *Small* **2023**, *20*, 2302721.
[34] X. Wen, Z. Lu, X. Yang, C. Chen, M. A. Washington, G.-C. Wang, J. Tang, Q. Zhao, T.-M. Lu, *ACS Appl. Mater. Interfaces* **2023**, *15*, 22251.
[35] P. Fan, G.-J. Chen, S. Chen, Z.-H. Zheng, M. Azam, N. Ahmad, Z.-H. Su, G.-X. Liang, X.-H. Zhang, Z.-G. Chen, *ACS Appl. Mater. Interfaces* **2021**, *13*, 46671.
[36] X. Liang, C. Guo, T. Liu, Y. Liu, L. Yang, D. Song, K. Shen, R. E. I. Schropp, Z. Li, Y. Mai, *Sol. RRL* **2020**, *4*, 2000294.
[37] P. Vidal-Fuentes, M. Placidi, Y. Sánchez, I. Becerril-Romero, J. Andrade-Arvizu, Z. Jehl, A. Pérez-Rodríguez, V. Izquierdo-Roca, E. Saucedo, *Sol. RRL* **2020**, *4*, 2000141.
[38] X. Liu, Y. Qiao, Y. Liu, J. Liu, E. Jia, S. Chang, X. Shen, S. Li, K. Cheng, *Sol. Energy* **2020**, *195*, 697.
[39] X. Liu, X. Xiao, Y. Yang, D.-J. Xue, D.-B. Li, C. Chen, S. Lu, L. Gao, Y. He, M. C. Beard, G. Wang, S. Chen, J. Tang, *Prog. Photovoltaics: Res. Appl.* **2017**, *25*, 861.
[40] I. Barin, *Thermochemical Data of Pure Substances*, 3rd ed., Vol. *1*, VCH Verlagsgesellschaft mbH, New York, **1995**.
[41] M. Binnewies, E. Milke, *Thermochemical Data of Elements and Compounds*, Wiley, Hoboken, **2002**.
[42] W. M. Haynes, D. R. Lide, T. J. Bruno (Eds.), *CRC Handbook of Chemistry and Physics*, Vol. *1*, 97th ed., CRC Press, Boca Raton, **2017**.
[43] W. Xu, Q. Song, G. Song, Q. Yao, *Thermochim. Acta* **2020**, *683*, 178480.
[44] A. Shongalova, M. R. Correia, B. Vermang, J. M. V. Cunha, P. M. P. Salomé, P. A. Fernandes, *MRS Commun.* **2018**, *8*, 1.
[45] R. Anandan, T. P. Xavier, M. Piraviperumal, *Mater. Chem. Phys.* **2024**, *322*, 129571.
[46] H. Zhou, M. Feng, K. Song, B. Liao, Y. Wang, R. Liu, X. Gong, D. Zhang, L. Cao, S. Chen, *Nanoscale* **2019**, *11*, 22871.
[47] A. Kumar, V. Kumar, A. Romeo, C. Wiemer, G. Mariotto, *J. Phys. Chem. C* **2021**, *125*, 19858.
[48] K. Nagata, K. Ishibashi, Y. Miyamoto, *Jpn J. Appl. Phys.* **1981**, *20*, 463.
[49] C. Platzer-Björkman, P. Zabierowski, J. Pettersson, T. Törndahl, M. Edoff, *Prog. Photovoltaics Res. Appl.* **2010**, *18*, 249.
[50] S. Ahn, K. H. Kim, J. H. Yun, K. H. Yoon, *J. Appl. Phys.* **2009**, *105*, 113533.
[51] Z. Chen, H. N. Dinh, E. Miller, *Photoelectrochemical Water Splitting: Standards, Experimental Methods, and Protocols*, 1st ed., Springer-Verlag, New York, **2013**.
[52] G.-X. Liang, Z.-H. Zheng, P. Fan, J.-T. Luo, J.-G. Hu, X.-H. Zhang, H.-L. Ma, B. Fan, Z.-K. Luo, D.-P. Zhang, *Sol. Energy Mater. Sol. Cells* **2018**, *174*, 263.
[53] Y. H. Kwon, M. Jeong, H. W. Do, J. Y. Lee, H. K. Cho, *Nanoscale* **2015**, *7*, 12913.
[54] D. Wang, D. Yu, M. Mo, X. Liu, Y. Qian, *J. Cryst. Growth* **2003**, *253*, 445.
[55] J. Singh, V. Verma, R. Kumar, R. Kumar, *Results Phys.* **2019**, *13*, 102106.
[56] A. Ajmi, K. Karoui, K. Khirouni, A. Ben Rhaiem, *RSC Adv.* **2019**, *9*, 14772.
[57] P. Norouzzadeh, Kh. Mabhouti, M. M. Golzan, R. Naderali, *Optik (Stuttg)* **2020**, *204*, 164227.

[58] J. F. Moulder, W. F. Stickle, P. E. Sobol, K. D. Bomben, *Handbook of X-ray Photoelectron Spectroscopy*, 2nd ed. (Ed: J. Chastain), Perkin-Elmer Corporation, Eden Prairie, **1992**.
[59] T. Meyer, A. Girard, M. Bouška, E. Baudet, M. Baillieul, P. Němec, V. Nazabal, C. Cardinaud, *Plasma Sources Sci. Technol.* **2023**, *32*, 085003.
[60] M. Luo, M. Leng, X. Liu, J. Chen, C. Chen, S. Qin, J. Tang, *Appl. Phys. Lett.* **2014**, *104*, 173904.
[61] A. K. Jain, C. Gopalakrishnan, P. Malar, *J. Mater. Sci.: Mater. Electron.* **2022**, *33*, 10430.
[62] S. Wen, X. Yin, H. Xie, Y. Guo, J. Liu, D. Liu, W. Que, H. Liu, W. Liu, *J. Adv. Dielectr.* **2020**, *10*, 2050016.
[63] F. A. Stevie, C. L. Donley, *J. Vac. Sci. Technol., A* **2020**, *38*, 063204.
[64] C. H. Don, H. Shiel, T. D. C. Hobson, C. N. Savory, J. E. N. Swallow, M. J. Smiles, L. A. H. Jones, T. J. Featherstone, P. K. Thakur, T.-L. Lee, K. Durose, J. D. Major, V. R. Dhanak, D. O. Scanlon, T. D. Veal, *J. Mater. Chem. C* **2020**, *8*, 12615.
[65] J. I. Langford, A. J. C. Wilson, *J. Appl. Crystallogr.* **1978**, *11*, 102.
[66] S. Kim, H. You, K. Yun, J. Kim, T. Seong, *Adv. Opt. Mater.* **2023**, *11*, 2201974.
[67] P. Vidal-Fuentes, M. Guc, I. Becerril-Romero, D. Sylla, X. Alcobé, Y. Sánchez, A. Pérez-Rodríguez, E. Saucedo, V. Izquierdo-Roca, *Sol. RRL* **2021**, *5*, 2100517.
[68] S. Lopez-Marino, M. Espíndola-Rodríguez, Y. Sánchez, X. Alcobé, F. Oliva, H. Xie, M. Neuschitzer, S. Giraldo, M. Placidi, R. Caballero, V. Izquierdo-Roca, A. Pérez-Rodríguez, E. Saucedo, *Nano Energy* **2016**, *26*, 708.
[69] A. Mavlonov, T. Razykov, F. Raziq, J. Gan, J. Chantana, Y. Kawano, T. Nishimura, H. Wei, A. Zakutayev, T. Minemoto, X. Zu, S. Li, L. Qiao, *Sol. Energy* **2020**, *201*, 227.
[70] S.-N. Park, S.-Y. Kim, S.-J. Lee, S.-J. Sung, K.-J. Yang, J.-K. Kang, D.-H. Kim, *Mater. Adv.* **2022**, *3*, 978.
[71] J. Y. Kim, P. Lindgren, Y.-J. Zhang, S. K. Kim, T. M. Valentin, H.-T. Jung, A. A. Peterson, *Mater. Adv.* **2021**, *2*, 4867.
[72] M. B. Costa, M. A. de Araújo, R. Paiva, S. A. Cruz, L. H. Mascaro, *J. Chem. Eng.* **2024**, *485*, 149526.
[73] C. Batchelor-McAuley, *Curr. Opin. Electrochem.* **2023**, *37*, 101176.
[74] S. Chen, T. Liu, Z. Zheng, M. Ishaq, G. Liang, P. Fan, T. Chen, J. Tang, *J. Energy Chem.* **2022**, *67*, 508.
[75] Y. Wang, Y. Chen, Y. Yun, X. Hong, Y. Huang, H. Ji, *Appl. Catal., B* **2024**, *358*, 124375.
[76] X. Chen, X. Li, Y. Peng, H. Yang, Y. Tong, M.-S. Balogun, Y. Huang, *Adv. Funct. Mater.* **2024**, *25*, 2416091.
[77] J. H. Kim, J. S. Lee, *Adv. Mater.* **2019**, *31*, 1970146.
[78] K. Lee, T.-H. Kim, S.-H. Jo, S. Yu, *Chemosphere* **2024**, *354*, 141675.
[79] D. Klotz, D. A. Grave, A. Rothschild, *Phys. Chem. Chem. Phys.* **2017**, *19*, 20383.
[80] K. J. Tiwari, M. Neuschitzer, M. Espíndola-Rodriguez, Y. Sánchez, Z. Jehl, P. Vidal-Fuentes, E. Saucedo, P. Malar, *Sol. Energy Mater. Sol. Cells* **2020**, *215*, 110603.
[81] M. Bär, B.-A. Schubert, B. Marsen, S. Krause, S. Pookpanratana, T. Unold, L. Weinhardt, C. Heske, H.-W. Schock, *Appl. Phys. Lett.* **2011**, *99*, 152111.
[82] D.-C. Nguyen, K. Fukatsu, K. Tanimoto, S. Ikeda, M. Matsumura, S. Ito, *Int. J. Photoenergy* **2013**, *2013*, 1.
[83] M. E. Erkan, V. Chawla, I. Repins, M. A. Scarpulla, *Sol. Energy Mater. Sol. Cells* **2015**, *136*, 78.
[84] Y. Guo, J. Jiang, S. Zuo, F. Shi, J. Tao, Z. Hu, X. Hu, G. Hu, P. Yang, J. Chu, *Sol. Energy Mater. Sol. Cells* **2018**, *178*, 186.
[85] O. Vigil-Galán, J. A. Andrade-Arvizu, M. Courel-Piedrahita, C. Mejía-García, E. Valencia-Resendíz, Y. Sánchez-González, M. Espíndola-Rodríguez, E. Saucedo-Silva, R. González-Castillo, E. Rodríguez-González, D. Seuret-Jiménez, D. Jiménez-Olarte, *J. Mater. Sci.: Mater. Electron.* **2017**, *28*, 18706.
[86] X. Zhang, G. Lu, Y. Wu, J. Dong, C. Wang, *Catal. Sci. Technol.* **2021**, *11*, 5505.
[87] K. T. Fountaine, H. J. Lewerenz, H. A. Atwater, *Nat. Commun.* **2016**, *7*, 1.
[88] C. A. Schneider, W. S. Rasband, K. W. Eliceiri, *Nat. Methods* **2012**, *9*, 671.
[89] L. Zeng, Z. Zhao, F. Lv, Z. Xia, S.-Y. Lu, J. Li, K. Sun, K. Wang, Y. Sun, Q. Huang, Y. Chen, Q. Zhang, L. Gu, G. Lu, S. Guo, *Nat. Commun.* **2022**, *13*, 3822.
[90] R. R. Prabhakar, T. Moehl, S. Siol, J. Suh, S. D. Tilley, *Chem. Mater.* **2020**, *32*, 7247.
[91] N. Fairley, V. Fernandez, M. Richard-Plouet, C. Guillot-Deudon, J. Walton, E. Smith, D. Flahaut, M. Greiner, M. Biesinger, S. Tougaard, D. Morgan, J. Baltrusaitis, *Appl. Surf. Sci. Adv.* **2021**, *5*, 100112.
[92] M. Nowak, B. Kauch, P. Szperlich, *Rev. Sci. Instrum.* **2009**, *80*, 1.
[93] P. Makuła, M. Pacia, W. Macyk, *J. Phys. Chem. Lett.* **2018**, *9*, 6814.
[94] L. Dejam, J. Sabbaghzadeh, A. Ghaderi, S. Solaymani, R. S. Matos, Ş. Ţălu, H. D. da Fonseca Filho, A. H. Sari, H. Kiani, A. H. S. shayegan, M. A. Doudaran, *Sci. Rep.* **2023**, *13*, 6518.
[95] L. Wang, C. Lee, P. Schmuki, *J. Mater. Chem. A* **2013**, *1*, 212.